HMGN5 promotes renal tubular inflammation and pyroptosis-associated signaling in chronic kidney disease via the IFNAR2 axis

XUE RONG[1,2*], JING XU[2*], JIENAN ZHANG[2], QI ZHANG[2], JIANGLI WANG[2], GUOXIN ZHANG[2] and LIMIN NIE[2]

[1]Medical Administration Office, Shijiazhuang People's Hospital, Shijiazhuang, Hebei 050011, P.R. China;
[2]Department of Nephrology, Shijiazhuang People's Hospital, Shijiazhuang, Hebei 050011, P.R. China

Received December 21, 2025; Accepted September 21, 2026

DOI: 10.3892/ijmm.2026.6022

Abstract. Chronic kidney disease (CKD) is a condition that is characterized by persistent tubular injury, inflammation and progressive fibrosis, ultimately leading to an irreversible loss of renal function. Pyroptosis, a notably pro-inflammatory mode of programmed cell death, contributes to tubular epithelial injury and amplifies renal inflammwation. The present study investigated the role of high mobility group nucleosome-binding protein 5 (HMGN5) in CKD and its regulatory relationship with interferon (IFN) receptor 2 (IFNAR2) signaling. The present study found that HMGN5 expression was significantly upregulated in renal tissues obtained from patients with CKD and CKD-model mice; this upregulation was accompanied by enhanced renal injury, fibrosis and inflammatory cytokine production. *In vitro*, HMGN5 overexpression in HK-2 cells: i) Promoted the expression of IFNAR2, phosphorylated-interferon regulatory factor (IRF)3/IRF7 and absent in melanoma 2; ii) enhanced the cleavage of caspase-1 and gasdermin D; iii) increased IL-1β, IL-8 and IFN-β secretion; and iv) promoted lactate dehydrogenase release. These findings suggested the activation of pyroptosis-associated cellular responses. Conversely, silencing HMGN5 or blocking IFNAR2 signaling markedly attenuated these effects. *In vivo*, pharmacological blockade of IFNAR2 ameliorated renal tissue damage, reduced fibrosis, restored renal function, decreased systemic cytokine levels and suppressed pyroptosis-associated signaling in CKD-model mice. Collectively, the findings of the present study identified HMGN5 as a novel regulator of IFNAR2-related pyroptosis-associated signaling in renal tubular epithelial cells and suggested that the HMGN5-IFNAR2 axis represents a pathophysiological pathway of interest in CKD that warrants further investigation.

Correspondence to: Professor Limin Nie, Department of Nephrology, Shijiazhuang People's Hospital, 365 Jianhua South Street, Yuhua, Shijiazhuang, Hebei 050011, P.R. China
E-mail: 90080106@hebmu.edu.cn

*Contributed equally

Key words: chronic kidney disease, high mobility group nucleosome-binding protein 5, interferon receptor 2 signaling, pyroptosis

Introduction

Chronic kidney disease (CKD) represents a notable global health burden and is characterized by progressive structural and functional damage to the kidneys, ultimately leading to the irreversible loss of renal function, including waste clearance, water-electrolyte and acid-base homeostasis, and endocrine regulation (1). Driven by the rising prevalence of population aging, which causes progressive nephron loss, alongside hypertension and diabetes, which induce microvascular damage and glomerular hyperfiltration, CKD has emerged as a mounting challenge to global healthcare systems (1,2). Additionally, patients with CKD frequently experience systemic complications, which markedly increase cardiovascular risk and reduce patient quality of life (2,3). Although renal replacement therapies, such as dialysis and transplantation, can prolong patient survival, their efficacy remains limited by prohibitive financial burdens, severe treatment-related complications and persistent disparities in global accessibility (3,4). Therefore, identifying the molecular mechanisms driving CKD progression and exploring the underlying pathophysiology of this disease are important for developing strategies to delay CKD advancement.

Inflammatory responses and regulated cell death are processes that are central to CKD progression and renal interstitial fibrosis (5). Among these processes, pyroptosis-associated signaling cascades, which trigger cellular stress and amplify inflammation, have attracted increasing attention (6). For instance, a previous study demonstrated that canonical pyroptosis can be initiated by inflammasome activation, such as via absent in melanoma 2 (AIM2) or NLR family pyrin domain containing 3 (NLRP3), leading to caspase-1 cleavage and subsequent gasdermin (GSDM)D-mediated cellular responses, which promote IL-1β and IL-18 release and amplify inflammation (6,7). Notably, while a previous study highlighted the role of the NLRP3 inflammasome in metabolic inflammation (8), accumulating evidence has further

demonstrated that interferon (IFN) signaling possesses a highly specific, well-documented evolutionary link with the AIM2 inflammasome pathway (9-11). Consistent with this, in CKD, IFN signaling transcriptionally upregulates AIM2, while cell stress-released aberrant cytosolic dsDNA activates this sensor, together driving GSDM-mediated PANoptosis and renal inflammation/fibrosis that perpetuate CKD progression (12-14). These findings highlight an important role for IFN signaling in connecting cell stress or inflammatory cues to pyroptosis-associated cell injury in renal and non-renal tissues.

The high mobility group nucleosome-binding (HMGN) protein family represents a class of chromatin architectural regulators that modulate transcription by altering nucleosome accessibility (15,16). HMGN1 has been reported to act as an alarmin, enhancing innate immune responses through IFN regulatory factor (IRF)3/IRF7-dependent type I IFN induction (17). HMGN5 shares structural similarity with HMGN1 and may exert analogous regulatory effects, but its role in CKD remains ambiguous (16). Chromatin remodeling is important in CKD, as it helps sustain a proinflammatory and profibrotic transcriptional program in renal tubular epithelial cells (18,19). We hypothesize that HMGN5 may function as an upstream epigenetic regulator that links chromatin remodeling to IFN signaling, potentially contributing to inflammasome activation and pyroptosis-associated cellular responses in renal tubular epithelial cells.

To test this hypothesis, the present study systematically examined HMGN5 expression in CKD, assessed its role in renal tubular injury and explored its regulatory effects on the transcription and signaling of key pyroptosis-related genes. The present study aimed to provide mechanistic insight into the HMGN5-IFN-pyroptosis axis and explore its potential as a pathophysiological pathway of interest for limiting renal injury.

Materials and methods

Human renal tissue collection and grouping. A total of 45 participants recruited between April 2024 and May 2025 were enrolled in the present study at Shijiazhuang People's Hospital (Shijiazhuang, China), comprising 20 individuals in the control group and 25 patients in the CKD group. The control group consisted of 12 male patients and 8 female patients, with a median age of 46 years (range, 35-62 years). The CKD group comprised 14 male patients and 11 female patients, with a median age of 54 years (range, 42-71 years). Detailed clinical and pathological characteristics of these patients, including age, sex, CKD stage (classified according to the KDIGO clinical practice guidelines) (20), renal function (estimated glomerular filtration rate), underlying etiology and comorbidities, have been summarized in Table I.

In the disease group, renal tissue specimens were collected from patients with CKD who underwent diagnostic biopsy or surgical intervention. Control renal tissues were obtained from patients who were hospitalized and undergoing radical or partial nephrectomy for renal tumors, with samples taken from non-tumorous renal cortical regions located at least 2 cm away from the tumor margin. To ensure the integrity of the control group, all control samples were independently evaluated by two experienced pathologists and confirmed to be free of glomerulosclerosis, tubular atrophy, interstitial fibrosis or active inflammatory lesions, and were thus considered histologically normal. Additional inclusion criteria for the control group included normal renal function and the absence of structural renal abnormalities; furthermore, patients with a clinical history of hypertension or diabetes mellitus were excluded from the control group to minimize confounding systemic effects. The CKD and control groups were approximately age- and sex-matched.

All human tissue collection procedures were conducted in accordance with the Declaration of Helsinki. Written informed consent for the use of resected renal tissues in this scientific research was obtained from all participants or in cases where patients were unable to communicate or incapacitated, from their designated legal representatives, and the study protocol was approved by the Medical Scientific Research Ethics Committee of Shijiazhuang People's Hospital (Shijiazhuang, China; approval no. 2023-56A). Upon excision, renal tissues were processed immediately: One portion of these tissues was fixed in 4% paraformaldehyde at room temperature for 24 h for histological and immunofluorescence analysis, whereas the remaining sample was snap-frozen in liquid nitrogen and stored at -80˚C for molecular assays.

Animals and experimental design. Specific pathogen-free male C57BL/6 mice purchased from Beijing Vital River Laboratory Animal Technology Co., Ltd. (Beijing, China) (aged 6-8 weeks; body weight, 20-25 g, a total of 18 mice) were used for *in vivo* animal experiments. Mice were housed under standard conditions (temperature, 22±2˚C; humidity, 50±10%; 12-h light/dark cycle) with *ad libitum* access to food and water. All animal procedures were approved by the Medical Scientific Research Ethics Committee of Shijiazhuang People's Hospital (approval no. 2024-99). Investigators were blinded to group allocation during data collection and analysis.

Surgical procedure and CKD induction. Chronic renal failure was induced via a two-step nephrectomy. In the first step, a left total nephrectomy was performed via a flank incision. A total of 1 week later, a right partial (2/3) nephrectomy was performed by ligating and resecting the upper and lower poles. Sham-operated mice underwent identical surgical exposure without tissue resection. Anesthesia for all surgical and invasive procedures was induced with 3-4% isoflurane and maintained with 1.5-2.0% isoflurane in oxygen. The depth of anesthesia was carefully monitored by checking the pedal withdrawal reflex and respiratory rate. To ensure post-operative analgesia and animal welfare, meloxicam (purity, 99.59%; cat. no. HY-B0261; MedChemExpress) was administered subcutaneously at a dose of 2 mg/kg immediately following the surgical procedures and once daily for 3 days thereafter. Meloxicam was dissolved in a vehicle comprising 10% DMSO, 40% polyethylene glycol 300, 5% Tween-80 and 45% saline, following the manufacturer's recommended protocol for *in vivo* studies. Mice were monitored daily for distress, and body weight was recorded twice weekly. Predefined humane endpoints included rapid weight loss exceeding 20% of baseline body weight, severe lethargy, inability to access food or water, or signs of unmanaged pain. During the experimental period, no animals met these humane endpoints.

Table I. Baseline clinical and pathological characteristics of the study population.

Characteristics	Control group (n=20)	CKD group (n=25)	P-value
Age (years), mean ± SD	47.2±8.5	53.8±9.2	0.746
Sex, n (%)			0.789
Male	12 (60.0)	14 (56.0)	
Female	8 (40.0)	11 (44.0)	
Serum creatinine (μmol/l), mean ± SD	74.3±12.5	284.6±78.3	<0.001
eGFR (ml/min/1.73 m^2), mean ± SD	96.4±10.8	22.8±6.5	<0.001
24-h urinary protein (g/24 h), mean ± SD	0.09±0.05	2.45±1.12	<0.001
CKD stage, n (%)			
Stage 3		6 (24.0)	
Stage 4		11 (44.0)	
Stage 5		8 (32.0)	
Underlying renal disease, n (%)			
lgA nephropathy	0 (0.0)	9 (36.0)	
Membranous nephropathy	0 (0.0)	6 (24.0)	
Diabetic kidney disease	0 (0.0)	7 (28.0)	
Hypertensive nephrosclerosis	0 (0.0)	3 (12.0)	
Comorbidities, n (%)			
Hypertension	0 (0.0)	21 (84.0)	<0.001
Diabetes mellitus	0 (0.0)	8 (32.0)	0.026
Hyperlipidemia	0 (0.0)	11 (44.0)	0.038

CKD, chronic kidney disease; eGFR, estimated glomerular filtration rate; IgA, immunoglobulin A; SD, standard deviation.

Grouping and baseline assessment. To validate the CKD model, serial blood samples (strictly restricted to 4 and 8 weeks post-surgery; 150-200 μl) were collected via the lateral saphenous vein at two experimental time points: At 4 weeks post-surgery (when mice were separated into treatment groups) to confirm the successful induction of the CKD model, and at the experimental endpoint (8 weeks post-surgery; prior to euthanasia) for comprehensive biochemical analysis, including measurements of serum creatinine and blood urea nitrogen levels (and no other blood biochemical assays were performed). This minimally invasive blood-collection method was chosen to avoid the severe stress and injury that is associated with more invasive blood-collection techniques (such as retro-orbital bleeding), thereby maintaining the physiological stability of the vulnerable CKD model by minimizing confounding stress responses. Mice were gently restrained for this procedure, and no anesthesia was required. The blood samples were allowed to clot at room temperature for 30 min, followed by centrifugation at 1,500 x g for 15 min at 4˚C to isolate serum, which was stored at -80˚C until analysis. At 4 weeks post-surgery, mice were randomly assigned into the following three groups (n=5 per group) using a random number table: Control, model + IgG and model + IFN receptor (IFNAR)-neutralizing antibody (IFNAR Ab). Statistical analysis indicated no significant differences in baseline renal function among these groups (P>0.05).

Intervention strategy. To investigate the role of IFNAR signaling in driving chronic renal inflammation and fibrosis during CKD pathogenesis, mice were treated with an IFNAR Ab (cat. no. BE0241; clone, MAR1-5A3; Bio X Cell; diluted in InVivoPure pH 7.0 buffer to a working dose of 200 μg in 100 μl per injection), which has been shown to effectively block downstream IFNAR signaling (21,22), for 4 weeks (250 μg/dose; intraperitoneal administration; three times per week, optimized to ensure sustained receptor saturation throughout the chronic disease model), as previously described (21,22). Mice in the control group received an equivalent dose of isotype-matched IgG (cat. no. BE0083; Bio X Cell; prepared and diluted to match the identical concentration) administered on the same schedule. This antibody treatment continued for 4 weeks. At the experimental endpoint, a larger volume of blood (0.8-1.0 ml) was collected via cardiac puncture under deep anesthesia (5% isoflurane) immediately prior to euthanasia to facilitate comprehensive biochemical analysis. Following blood collection, firm pressure was applied to the cardiac puncture site to ensure complete hemostasis. As a terminal workflow, exsanguination via cardiac puncture under deep anesthesia (5% isoflurane) served as the primary procedure, and mice were subsequently subjected to cervical dislocation as a confirmatory secondary procedure to ensure death. The absence of heartbeat, cessation of respiratory rhythm and loss of corneal reflexes were verified in mice to confirm successful euthanasia. Kidney tissues were harvested for further evaluation.

Histological assessment. Human and mouse renal tissues were fixed in 4% paraformaldehyde at room temperature for 24 h, followed by cryoprotection and embedding in an optimal

cutting temperature compound. Prior to embedding, tissue samples were stored in liquid nitrogen (-196˚C). Frozen sections (8 μm) were prepared using a cryostat at -20˚C and mounted onto glass slides. For each experimental group (n=5), three independent serial sections per kidney sample were prepared. Hematoxylin and eosin (H&E) staining was performed using a commercial kit (cat. no. G1120; Beijing Solarbio Science & Technology Co., Ltd.) according to the manufacturer's instructions. Briefly, sections were stained with hematoxylin at room temperature for 5 min, differentiated using 1% hydrochloric acid alcohol, rinsed in tap water followed by incubation in PBS for bluing, and counterstained with eosin at room temperature for 2 min. After dehydration in graded ethanol and clearing in xylene, sections were mounted with neutral resin. Slides were examined using a light microscope (x20 magnification; Keyence Corporation).

Assessment of renal tubular injury. As an extension of the aforementioned histological analysis, renal tubular injury was specifically evaluated in mouse kidney samples. To semi-quantify renal tubular injury, three independent serial sections were prepared for each kidney sample (n=5) as aforementioned. For each section, images of 10 random fields were captured at x20 magnification using a light microscope. All images were acquired using identical settings to ensure inter-group comparability. Any post-acquisition adjustments to brightness or contrast were applied uniformly to the entire image and across all comparative groups. Renal tubular injury was assessed by two blinded investigators using a semi-quantitative scale (0-4), based on the extent of tubular dilation, urinary cast formation and epithelial sloughing; the grading system was as follows: 0, no damage; 1, <25% of the tubular area was affected; 2, 25-50% of the tubular area was affected; 3, 50-75% of the tubular area was affected; and 4, >75% of the tubular area was affected. Any discrepancies in scoring between the two investigators were resolved by re-evaluating the slide together to reach a consensus, or by consulting a third senior pathologist when necessary. The average injury score was calculated for each mouse to represent the overall degree of renal injury.

Masson's trichrome staining. To evaluate renal fibrosis in mouse kidney samples, three independent serial sections (8 μm) of frozen renal tissue were prepared using a cryostat set at -20˚C and stained using a Masson's Trichrome Stain Kit (cat. no. G1340; Beijing Solarbio Science & Technology Co., Ltd.) according to the manufacturer's protocol. Briefly, sections were fixed in saturated aqueous Bouin's solution (commercially provided in the kit) at room temperature overnight, followed by rinsing in 75% ethanol until the yellow coloration was removed. Cytoplasmic and muscle fibers were stained with ponceau-fuchsin solution at room temperature for 10 min. Subsequently, sections were treated with phosphomolybdic acid for differentiation at room temperature for 5 min and stained with aniline blue at room temperature for 5 min to label collagen fibers. Finally, sections were dehydrated, cleared in xylene and mounted with neutral resin.

Quantification of renal fibrosis. To evaluate the degree of tubulointerstitial fibrosis in mouse kidney samples, three independent serial sections were prepared for each kidney sample (n=5) as aforementioned. For each section, images of 10 random fields (excluding major blood vessels and large renal corpuscles to ensure evaluation of the tubulointerstitial area) were captured at x20 magnification using a light microscope (Keyence Corporation). To ensure inter-group comparability, all images were acquired under identical settings (including exposure time, gain and brightness). The fibrotic area (blue-stained collagen) for each field was quantified using ImageJ software (version 1.53k; National Institutes of Health). A standardized color thresholding protocol (with fixed hue, saturation and brightness parameters consistently applied across all experimental groups) was applied to distinguish collagen fibers from background and non-fibrotic tissue. To avoid potential confounding effects from non-specific luminal staining or casts, tubular lumens were strictly masked and excluded during the quantitative measurement. The extent of fibrosis was expressed as the percentage of the blue-stained area relative to total tubulointerstitial tissue area (excluding tubular lumens) per field. All assessments were performed by two blinded investigators (who were kept unaware of the experimental group assignments during image selection, threshold setup and quantitative measurements to eliminate observer bias). Any discrepancies between the two investigators were resolved by re-evaluating the images together to reach a consensus, or by consulting a third senior researcher. The mean value of the fibrotic area for each mouse was used for statistical analysis.

Immunofluorescence. For histological analysis via immunofluorescence, three independent serial renal tissue sections were prepared for each mouse kidney sample (n=5). For paraffin-embedded tissues, samples were fixed in 4% paraformaldehyde at room temperature for 24 h and sectioned at a thickness of 4 μm using a microtome. Sections were then deparaffinized in xylene, rehydrated through a descending ethanol series, and subjected to antigen retrieval using a specific buffer (citrate buffer, pH 6.0), followed by blocking with 5% bovine serum albumin (BSA; Beijing Solarbio Science & Technology Co., Ltd.) at room temperature for 1 h to minimize non-specific binding. Cultured cells on coverslips were rinsed with phosphate-buffered saline (PBS), fixed with 4% paraformaldehyde at room temperature for 15 min and permeabilized with 0.1% Triton X-100 at room temperature for 10 min, followed by blocking with 5% BSA at room temperature for 1 h.

Both tissue sections and cells were then incubated with primary antibodies against connective tissue growth factor (CTGF; cat. no. ab6992; Abcam; 1:200), IRF3 (cat. no. ab68481; Abcam; diluted 1:200) and IRF7 (clone SC0617; cat. no. MA5-41165; Invitrogen; 1:150) overnight at 4˚C, followed by incubation with appropriate ActivAbTMMouse Anti-Rabbit IgG(8A3)/Solar Fluor 568 (Beijing Solarbio Science & Technology Co., Ltd.; 1:500) in the dark at room temperature for 1 h. Nuclei were counterstained with DAPI (Beijing Solarbio Science & Technology Co., Ltd.) at room temperature for 5 min. Samples were mounted with an anti-fade medium and images were captured using a fluorescence microscope (Keyence Corporation).

Quantitative image analysis. For histological samples, analysis was performed on three independent serial sections per kidney (n=5). For cell cultures, experiments were performed in three independent biological replicates. In both cases, images were captured of 10 random fields per tissue section or per cell coverslip at x20 magnification under identical acquisition settings (exposure time, gain and intensity). Any image adjustments, including global background subtraction, brightness or contrast, were applied uniformly across all experimental groups without altering specific regional signals.

For analyzing CTGF (evaluated as a key downstream pro-fibrotic effector regulated by TGF-β and IFN signaling pathways, serving as a classic marker reflecting extracellular matrix remodeling and tubulointerstitial fibrosis progression in CKD), mean fluorescence intensity was quantified using ImageJ software (version: 1.54k, National Institutes of Health) by applying standardized thresholding. For IRF3 and IRF7 analysis, the extent of nuclear translocation was assessed by calculating the nuclear-to-cytoplasmic fluorescence ratio, with DAPI defining the nuclear mask. Data are expressed as the mean nuclear-to-cytoplasmic ratio. All analyses were conducted by two blinded investigators to minimize observation bias, and any quantitative discrepancies between the two investigators exceeding a predetermined 10% threshold were resolved by consultation with a third senior investigator, and the final value for each mouse (serving as an independent biological replicate) was determined by the mean values of the captured fields. All data are presented as the mean of three independent biological replicates.

Cell culture. The human renal proximal tubular epithelial cell line HK-2 (Procell Life Science & Technology Co., Ltd.) was cultured in Minimum Essential Medium supplemented with non-essential amino acids (cat. no. PM150410; Procell Life Science & Technology Co., Ltd.), 10% fetal bovine serum (cat. no. 164210; Procell Life Science & Technology Co., Ltd.) and 1% penicillin-streptomycin (cat. no. PB180120; Procell Life Science & Technology Co., Ltd.). The authenticity of the HK-2 cell line was verified by short tandem repeat profiling analysis provided by the supplier. All experimental procedures were conducted using cells within a restricted passage range (passages 5-15) to ensure phenotypic stability and consistency. Furthermore, the cultures were routinely screened and confirmed to be strictly negative for mycoplasma contamination. Cells were maintained at 37˚C in a humidified incubator with an atmosphere of 95% air and 5% CO_2. Culture medium was replaced every 2-3 days, and cells were passaged at 70-80% confluence using standard trypsinization procedures.

Adenoviral transduction. Recombinant adenoviruses were generated using the pAdEasy system, with homologous recombination performed in BJ5183 bacteria and subsequent rescue in HEK293 packaging cells (Cell Bank of the Chinese Academy of Sciences). Transfection into packaging cells was conducted using standard liposome-mediated transfection at 37˚C for 6 h, followed by viral particle expansion, collection and purification. To manipulate the expression of HMGN5 or IFNAR in HK-2 cells, adenoviral vectors were employed. For HMGN5 overexpression, the HMGN5 coding sequence was cloned into the pAdEasy-CMV-ZsGreen backbone (custom-synthesized based on standard pAdEasy framework; equivalent backbone details available via Agilent Technologies, Inc.; cat. no. 240009) to generate the HMGN5 overexpression vector (Ad-HMGN5), with the empty vector serving as the negative control for overexpression (Ad-NC). For knockdown experiments, short hairpin RNA (shRNA) sequences targeting HMGN5 (5'-TCTATAGGAGATCTTAGTCAG-3') or IFNAR2 (5'-TTATTCCTCCTATTTTGGCAG-3') were cloned into the pAdEasy-U6-EGFP backbone (custom-synthesized based on standard pAdEasy framework; equivalent backbone details available via Agilent Technologies, Inc.; cat. no. 240021), as well as a scrambled negative control shRNA sequence (Ad-sh-NC; 5'-TTCTCCGAACGTGTCACGT-3'). All adenoviral vectors were designed and synthesized by Suzhou GenePharma Co., Ltd. For transduction, HK-2 cells were seeded in culture plates at a seeding density of $2x10^5$ cells/well and incubated at 37˚C for 24 h and allowed to reach ~80% confluence. The culture medium was then replaced with fresh medium containing the respective adenoviruses at a multiplicity of infection of 20. After 8 h of incubation at 37˚C in a humidified atmosphere with 5% CO_2, the virus-containing medium was aspirated and replaced with complete fresh medium. Cells were further cultured for 48 h to allow for efficient transgene expression or knockdown.

Reverse transcription-quantitative PCR (RT-qPCR). Total RNA was extracted from renal tissues or cultured HK-2 cells (including both control and adenoviral-transduced cells) using TRIzol® reagent (Invitrogen; Thermo Fisher Scientific, Inc.) for extraction or an equivalent method according to the manufacturer's instructions of both the TRIzol reagent and the RT kit. RT-qPCR was performed using a One-Step RT-PCR Kit (Beyotime Biotechnology; cat. no. HKE045-01A; utilizing SYBR Green as the fluorophore), which allowed RT and PCR amplification to be carried out in a single reaction strictly according to the manufacturer's protocol. Briefly, RNA templates, primers, 2X One-Step RT-PCR SuperMix, RT Enzyme Mix and RNase-free water were thawed on ice prior to use. The PCR reaction was prepared at a total volume of 20 μl, containing 1 μg RNA template, 10 μl 2X One-Step RT-PCR SuperMix, 1 μl RT Enzyme Mix, 1 μl each of forward and reverse primers (10 μM), and RNase-free water to volume. The reaction mixture was gently mixed and briefly centrifuged at 12,000 x g at 4˚C for 30 sec to collect the contents at the bottom of the tube. RT and PCR amplification were performed using the following thermal cycling conditions: initial RNA denaturation at 65˚C for 5 min, followed by RT at 42˚C for 5 min, final enzyme inactivation at 85˚C for 5 min and initial denaturation at 95˚C for 5 min, followed by 25-30 cycles of denaturation at 94˚C for 20 sec, annealing at 50-60˚C for 20 sec and extension at 72˚C for 60 sec per kilobase, with a final extension step at 72˚C for 5 min. The reaction was then held at 4˚C indefinitely to preserve sample stability prior to analysis. The mRNA expression levels of HMGN5, IL-1β, IL-18 and IL-6 were subsequently analyzed. Gene expression was normalized to an internal reference gene (β-actin), and relative expression levels were calculated using the $2^{-\Delta\Delta Cq}$ method (23). All reactions were performed with technical replicates (n=3) per group), and independent biological replicates were included according to the experimental design. The primers used in this protocol have been listed in Table II.

Table II. Primers used in the present study.

A, RT-qPCR

Primer	Sequence (5'-3')
HMGN5	
Forward	TGTGAGTGAATTTCGTGTTGTGT
Reverse	ACCTGCAGAACAAGAATGTTGG
β-actin	
Forward	ACAGGAAGTCCCTTGCCATC
Reverse	TGTGTGGACTTGGGAGAGGA
IFN-β	
Forward	CTAGCACTGGCTGGAATGAGA
Reverse	TGGCCTTCAGGTAATGCAGA
IRF3	
Forward	TGGGCCCCCAGATCTGATTA
Reverse	AATCCATGCCCTCCACCAAG
IRF7	
Forward	CGGCACTAACGACAGGCG
Reverse	CGGCCCTTGTACATGATGGT

B, ChIP-qPCR

Primer	Sequence (5'-3')
IFNAR2	
Forward	TGCCTATCCCGAAACACGTTG
Reverse	TCCGTTGTAGATTCTCCCCTCT
AIM2	
Forward	TCATGGTCACGCTCTTTGGT
Reverse	CTTCAGCCCCACTTCCCATT
IFN-β	
Forward	GGCTGTGACTGGTTGGTTTG
Reverse	TGTGAGAGGGCCTTGGAAAC
IRF3	
Forward	GCCTAAGGAAGGCAGCTAGG
Reverse	GGAGTCCAGTCCCTAACCCT
IRF7	
Forward	TTCCGCTGGTCGCATCCAAT
Reverse	GCTTTTATGGTGGCCAGGCG

RT-qPCR, reverse transcription-quantitative PCR; ChIP-qPCR, chromatin immunoprecipitation-quantitative PCR; HMGN5, high mobility group nucleosome-binding 5; IFN-β, interferon-β; IRF3, interferon regulatory factor 3; IRF7, interferon regulatory factor 7; IFNAR2, interferon receptor 2; AIM2, absent in melanoma 2.

Western blotting. Total protein was extracted from renal tissues and cultured cells using a RIPA buffer (Beijing Solarbio Science & Technology Co., Ltd.) supplemented with protease and phosphatase inhibitors (Beijing Solarbio Science & Technology Co., Ltd.). Lysates were clarified by centrifugation at 12,000 x g for 15 min at 4˚C, and protein concentrations were determined using a BCA Protein Assay Kit (Beijing Solarbio Science & Technology Co., Ltd.) according to the manufacturer's instructions. A total of 30 μg of protein was loaded per lane.

All experiments were performed in at least three independent biological replicates. Equal amounts of protein were separated by SDS-PAGE and subsequently transferred onto PVDF membranes. After transfer, membranes were blocked with 5% bovine serum albumin (BSA; Beijing Solarbio Science & Technology Co., Ltd.) in Tris-buffered saline containing 0.1% Tween-20 (TBST) at room temperature to reduce non-specific binding. Membranes were then incubated with primary antibodies against HMGN5 (1:1,000; cat. no. ab186001; Abcam), AIM2 (1:1,000; cat. no. ab93015; Abcam), N-terminal pore-forming domain of GSDMD (GSDMD-N; 1:1,000; cat. no. ab215203; Abcam), GSDMD (1:1,000; cat. no. ab219800; Abcam), cleaved caspase-1 (1:1,000; cat. no. 89332; Cell Signaling Technology, Inc.), IFNAR2 (1:1,000; cat. no. ab193410; Abcam), phosphorylated (p-)IRF3 (1:1,000; cat. no. ab76493; Abcam), p-IRF7 (1:1,000; cat. no. 12390; Abcam) and β-actin (1:5,000; cat. no. 4967; Cell Signaling Technology, Inc.) overnight at 4˚C. Molecular weight markers were utilized to verify protein size. Following incubation with primary antibodies, membranes were washed with TBST and incubated with horseradish peroxidase (HRP)-conjugated secondary antibodies (goat anti-rabbit/mouse IgG, diluted at 1:5,000; cat. no. SE134/SE131; Beijing Solarbio Science & Technology Co., Ltd.) at room temperature for 1 h. Protein bands were visualized using an ECL Western Blotting Substrate (Beijing Solarbio Science & Technology Co., Ltd.) detection system and images were captured using a chemiluminescence imaging system. β-actin was used as an internal loading control. Band intensities were semi-quantified using ImageJ software (version 1.53t, National Institutes of Health) and normalized to the corresponding β-actin levels.

EdU cell proliferation assay. Cell proliferation was evaluated using the BeyoClick™ EdU-488 Cell Proliferation Kit (Beyotime Biotechnology). Transduced cells were seeded in 6-well plates at a density of $2x10^5$ cells/well and allowed to adhere overnight at 37˚C in a humidified incubator containing 5% CO_2 before experimental treatments. Cells were then incubated with EdU at a final concentration of 10 μM for 2 h at 37˚C. After labeling, cells were fixed with room-temperature 4% paraformaldehyde for 15 min, permeabilized with 0.3% Triton X-100 in PBS at room temperature for 15 min and subjected to click chemistry reactions according to the manufacturer's instructions provided with the aforementioned kit. Nuclei were counterstained with Hoechst 33342 (Beyotime Biotechnology) at room temperature for 10 min, and fluorescence images were captured using a fluorescence microscope. The proportion of EdU-positive cells was quantified using ImageJ software (version 1.53t, National Institutes of Health) to assess cell proliferation.

ELISA. IFN-β levels in cell culture supernatants (from HK-2 cells transfected with Ad-HMGN5 or Ad-NC for 24 h) and mouse plasma were measured using commercial ELISA kits for mouse (cat. no. SP13645) and human (cat. no. SP10123) IFN-β (Wuhan Saipei Biotechnology Co., Ltd.) according to the manufacturers' instructions. Samples and standards were

added to antibody-coated plates and incubated at 37˚C for 60 min, followed by incubation with biotin-labeled detection antibody at 37˚C for 30 min and streptavidin-HRP at 37˚C for 30 min (with thorough washing steps between each incubation). Color development was achieved using the TMB substrate solution provided in the kit (incubated in the dark at 37˚C for 15 min), and the reaction was terminated with stop solution. Absorbance was subsequently measured at 450 nm using a microplate reader (Thermo Fisher Scientific, Inc.). IFN-β concentrations were calculated based on standard curves.

Assessment of pyroptosis-associated signaling. To evaluate the involvement of pyroptosis-associated signaling in HMGN5-mediated renal-tubular injury, the present study employed a multi-parametric approach based on established molecular signatures (24,25). These molecular signatures and criteria were established based on well-documented literature defining gasdermin-mediated programmed cell death. In the present study, pyroptosis-associated signaling was defined by the confluence of the following criteria: i) Activation of the canonical inflammatory caspase cascade, specifically the presence of cleaved caspase-1; ii) proteolytic processing of GSDMD into GSDMD-N; iii) the maturation and release of pro-inflammatory cytokines, including IL-1β, IL-8 and IFN-β; and iv) the loss of plasma membrane integrity, as determined by the efflux of lactate dehydrogenase (LDH) into the culture supernatant (24,25). Although these markers collectively constitute a robust molecular signature of the pyroptotic pathway (24,25), the present study has referred to these findings as 'pyroptosis-associated signaling' throughout the manuscript to maintain rigor, as absolute morphological confirmation of this cell death modality, such as real-time visualization of membrane pore formation via transmission electron microscopy, was beyond the scope of the present study.

Chromatin immunoprecipitation (ChIP)-qPCR. To examine the direct binding of HMGN5 protein to specific genomic regions *in vivo*, ChIP-qPCR was performed using the Magna ChIP® A ChIP kit (cat. no. 17-610; Merck KGaA) according to the manufacturer's protocol. Briefly, HK-2 cells from the control, Ad-HMGN5 and Ad-NC groups were cross-linked using 1% formaldehyde for 10 min at room temperature. The reaction was subsequently quenched with 0.125 M glycine. After washing cell samples with cold PBS, cells were harvested and lysed sequentially using the cell lysis and nuclear lysis buffers provided in the kit. Chromatin was subsequently sheared by sonication (optimized to 15 cycles of 30 sec 'ON' and 30 sec 'OFF' on ice) to an average size of 200-1,000 bp. For immunoprecipitation, chromatin extracts equivalent to $1x10^6$ cells per IP reaction (derived from a total lysate input of normalized protein/cell concentration) were incubated overnight at 4˚C with 2 μg anti-HMGN5 antibody (cat. no. ab186001; 1:50; Abcam), normal IgG (negative control; cat. no. 12-371; 1:50; Merck KGaA). Protein A magnetic beads (20 μl per IP reaction) were then added and incubated at 4˚C for 2 h. Immune complexes were magnetically isolated using a magnetic separator rack. The immune complexes were subsequently washed extensively with the provided wash buffers. After reverse cross-linking (incubation at 65˚C for 2 h) and proteinase K digestion (incubation at 62˚C for 45 min), the co-precipitated DNA was purified. Enrichment of specific genomic regions was analyzed by qPCR using PowerUp™ SYBR™ Green Master Mix (Applied Biosystems; Thermo Fisher Scientific Inc.) and primers targeting the promoter/regulatory regions of the human IFNAR2 and AIM2 genes. The percentage of input chromatin was calculated using the formula: Input (%)=$2^{Cq(Input)-Cq(IP)}$ x dilution factor x100. Results have been presented as fold-enrichment relative to the IgG control. All experiments were performed in at least three independent biological replicates. The primers used have been listed in Table II.

Dual-luciferase reporter assay. The human *IFNAR2* promoter region containing the predicted HMGN5-binding site (identified by the ChIP assay) was amplified by PCR and cloned into the pGL3-basic firefly luciferase reporter vector (Promega Corporation) to generate the wild-type (WT) *IFNAR2* promoter-luciferase plasmid. A mutant construct, in which the core binding motif was disrupted, was generated using a site-directed mutagenesis kit (QuikChange II Site-Directed Mutagenesis Kit, cat. no. 200523; Agilent Technologies, Inc.). HK-2 cells were seeded in 24-well plates at a density of $1x10^5$ cells/well and co-transfected with the respective firefly luciferase reporter vectors (WT or mutant) and a pRL-TK *Renilla* luciferase plasmid (Promega Corporation) using Lipofectamine® 3000 (Thermo Fisher Scientific, Inc.) at 37˚C for 24 h, followed by transduction with Ad-NC or Ad-HMGN5 at an MOI of 50 at 37˚C for another 24 h (where transfection and transduction protocols were performed sequentially). After a total of 48 h of incubation at 37˚C, firefly and *Renilla* luciferase activities were sequentially measured using the Dual-Luciferase® Reporter Assay System (Promega Corporation) according to the manufacturer's protocol. Relative luciferase activity was calculated as the ratio of firefly luciferase intensity to *Renilla* luciferase intensity.

LDH cytotoxicity assay. Cell membrane integrity was evaluated using an LDH cytotoxicity assay kit (cat. no. C0016; Beyotime Biotechnology). HK-2 cells were seeded into 96-well plates at a density of $1x10^4$ cells/well and cultured until reaching 80-90% confluence. After HK-2 cells transfected with Ad-HMGN5, Ad-NC or Ad-sh-NC, Ad-sh-HMGN5 for 24 h, culture supernatants were collected to assess LDH release. Maximum LDH-release controls were generated by treating parallel wells with the LDH-release reagent provided in the kit. Following centrifugation at 400 x g for 5 min at room temperature, supernatants were transferred to a new 96-well plate and LDH activity was measured according to the kit manufacturer's instructions. LDH release was used as an indicator of cell membrane damage and cytotoxicity.

Caspase-1 activity assay. The enzymatic activity of caspase-1 in HK-2 cells (seeded at a density of $2x10^5$ cells/well in 6-well plates) was measured using a commercial Caspase-1 Activity Detection Kit (cat. no. C1102; Beyotime Biotechnology), strictly following the manufacturer's instructions. Briefly, HK-2 cells transfected with Ad-HMGN5, Ad-NC or Ad-sh-NC, Ad-sh-HMGN5 for 24 h were harvested and lysed using the provided lysis buffer on ice for 15 min.

After centrifugation at 16,000 x g at 4˚C for 15 min, the supernatant was collected and the protein concentration was quantified using the BCA method. Equal amounts of total protein (50 μg) were incubated with the specific synthetic substrate acetyl-Tyr-Val-Ala-Asp-p-nitroanilide at 37˚C for 4 h. Caspase-1 in the sample specifically cleaves the substrate to release the chromophore p-nitroaniline. The absorbance of the reaction mixture was measured at 405 μm using a microplate reader. The relative caspase-1 activity was normalized to the protein concentration of each sample, and the results were expressed as a fold change relative to the control group.

Statistical analysis. All quantitative data from experimental protocols are presented as the mean ± SEM. Regarding sample sizes, *in vivo* animal experiments were conducted with 5 mice per group and *in vitro* cellular assays were performed with three independent biological replicates. Statistical analyses were performed using GraphPad Prism 9.0 (Dotmatics). For baseline clinical and pathological characteristics (Table I), continuous variables are presented as mean ± SD, with data normality formally assessed using the Shapiro-Wilk test; normally distributed continuous variables were compared using an unpaired Student's t-test, whereas non-normally distributed continuous variables were compared using the Mann-Whitney U test, whereas categorical variables are presented as n (%) and compared using the χ^2 test or Fisher's exact test. For normally distributed continuous data meeting these assumptions, differences between two independent groups were analyzed using an unpaired two-tailed Student's t-test. Comparisons among three or more groups were evaluated using a one-way analysis of variance followed by Tukey's post-hoc test for multiple comparisons. For non-continuous or non-normally distributed data, such as renal injury scores, the Mann-Whitney U test was used for two-group comparisons, and the Kruskal-Wallis test followed by Dunn's post-hoc test was applied for comparisons among three or more groups. $P<0.05$ was considered to indicate a statistically significant difference. To ensure data transparency, exact P-values have been reported where appropriate, rather than solely indicating significance thresholds.

Results

HMGN5 is upregulated in CKD renal tissue. Histopathological analysis revealed marked structural alterations in renal tissues from patients with CKD compared with controls. Both H&E staining and Masson's trichrome staining demonstrated marked histological disruption and significantly increased fibrosis in the kidney tissues of patients with CKD, indicating severe pathological changes (Fig. 1A). Immunofluorescence staining showed that the expression of CTGF was significantly elevated in CKD renal tissues relative to controls (Fig. 1B). RT-qPCR analysis further revealed that HMGN5 mRNA was significantly upregulated in CKD tissues compared with controls (Fig. 1C). Consistently, western blot analysis demonstrated a significant increase in HMGN5 protein expression in renal tissue samples from patients with CKD relative to control tissues (Fig. 1D). Collectively, these data indicated that HMGN5 expression was significantly elevated at both the transcriptional and protein levels in the renal tissue of patients with CKD, in association with enhanced CTGF expression and notable histopathological alterations.

HMGN5 promotes pyroptosis-associated signaling in HK-2 cells. To investigate the functional impact of HMGN5 on pyroptosis-associated signaling, the present study manipulated its expression in HK-2 cells. Western blotting confirmed the efficiency of HMGN5 overexpression (Fig. 2A) and knockdown (Fig. 2C). RT-qPCR analysis showed that, compared with the control group, HMGN5 overexpression significantly upregulated the mRNA levels of IL-1β, IL-18 and IL-6 (Fig. 2B), whereas HMGN5 knockdown significantly suppressed the expression of these transcripts compared with controls (Fig. 2D).

Functionally, the present study assessed pyroptosis-associated cell injury using LDH release and caspase-1 activity assays. HMGN5 overexpression significantly increased LDH leakage (Fig. 2E) and caspase-1 enzymatic activity (Fig. 2F). Consistent with these findings, western blot analysis demonstrated that, compared with the control group, HMGN5 overexpression significantly elevated protein levels of AIM2, cleaved caspase-1 and GSDMD-N (Fig. 2G). Conversely, HMGN5 knockdown significantly reduced LDH release (Fig. 2H), caspase-1 activity (Fig. 2I) and the protein levels of AIM2, cleaved caspase-1 and GSDMD-N compared with the control group (Fig. 2J). Furthermore, EdU incorporation assays showed that HMGN5 knockdown significantly enhanced cell proliferation compared with controls (Fig. 2K), indicating that HMGN5 depletion alleviates growth inhibition associated with pyroptosis-related cellular stress. Taken together, these results demonstrated that HMGN5 promoted the activation of pyroptosis-associated signaling in HK-2 cells.

HMGN5 promotes IFN-β signaling and IRF3/IRF7 activation in HK-2 cells. To elucidate the mechanism underlying the HMGN5-mediated regulation of pyroptosis-associated signaling, the present study performed ChIP-qPCR assays to examine its enrichment at the promoters of HMGN5-target genes. The results showed that HMGN5 was significantly enriched at the *IFNAR2* promoter, whereas no significant level of enrichment was detected at the *IFNAR1 IRF3*, *IRF7* or *AIM2* promoters (Fig. 3A). To determine whether this promoter binding translated into functional transcriptional regulation, a dual-luciferase reporter assay was performed. Co-transfection with Ad-HMGN5 significantly increased the luciferase activity of the WT *IFNAR2* promoter reporter compared with the WT + Ad-NC group (Fig. 3B). Conversely, mutation of the predicted HMGN5-binding motif within the promoter constructs attenuated the HMGN5-induced enhancement of luciferase activity (Fig. 3B), providing further evidence that HMGN5 positively regulated *IFNAR2* transcription through direct promoter interactions. Furthermore, HMGN5 overexpression markedly increased the mRNA levels of *IFNAR2*, *IRF7* and *IRF3* compared with the control group (Fig. 3C), and significantly elevated IFN-β protein secretion as measured by ELISA (Fig. 3D). Additionally, LDH-release assays revealed that, compared with the control group, transduction with Ad-HMGN5 significantly increased LDH leakage in HK-2 cells (Fig. 3E), which was indicative of elevated cell-injury levels associated with pyroptosis-related signaling.

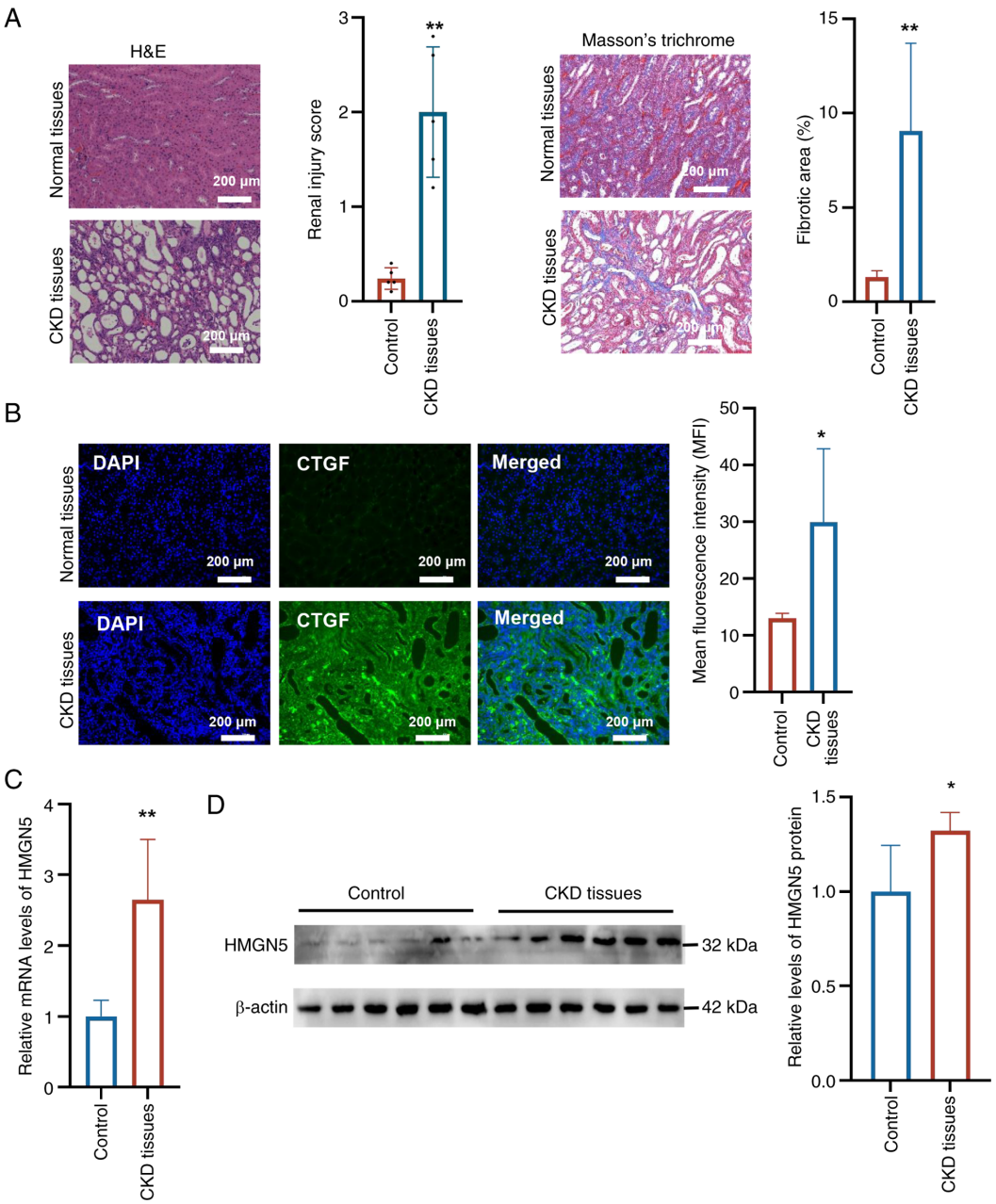


Figure 1. HMGN5 expression is elevated in CKD renal tissues. (A) Representative images of H&E staining and Masson's trichrome staining in renal tissues from patients with CKD and controls, accompanied by quantitative analysis of the renal injury score and fibrotic area. Scale bar, 200 μm. H&E staining was semi-quantified to calculate renal injury scores, and Masson's trichrome staining was used to quantify fibrosis in renal tissues. (B) Representative immunofluorescence staining images and fluorescence-intensity quantification comparing CTGF expression in renal tissues from patients with CKD with controls. Scale bar, 200 μm. (C) Reverse transcription-quantitative PCR analysis of HMGN5 mRNA levels in renal tissues from patients with CKD and controls. (D) Western blot analysis and semi-quantification of HMGN5 protein expression in renal tissues from patients with CKD and control samples. Data are presented as mean ± SEM (n=5 per group; 3 independent serial sections per sample). *P<0.05 and **P<0.01 vs. control. H&E, hematoxylin and eosin; HMGN5, high mobility group nucleosome-binding 5; CKD, chronic kidney disease; CTGF, connective tissue growth factor.

Western blot analysis further showed that, compared with controls, HMGN5 overexpression significantly upregulated the protein levels of IFNAR2, p-IRF3 and p-IRF7 (Fig. 3F), whereas HMGN5 knockdown resulted in a significant reduction in the expression levels of these markers (Fig. 3G). Furthermore, immunofluorescence staining demonstrated that, compared with the control group, HMGN5 overexpression significantly promoted the nuclear translocation of IRF3 and IRF7 in HK-2 cells (Fig. 3H and I), suggesting that HMGN5 modulated the IFN-β signaling cascade through transcriptional regulation of *IFNAR2*.

HMGN5 regulates pyroptosis-associated signaling via an IFNAR2-dependent mechanism. To investigate the role of IFNAR2 signaling in renal tubular epithelial cell injury, HK-2 cells were transduced with an adenovirus encoding an shRNA sequence targeting IFNAR2 (Ad-sh-IFNAR2). Compared with Ad-sh-NC-transduced cells, Ad-sh-IFNAR2 significantly reduced IFNAR2 expression. Concomitantly, the expression levels of AIM2, cleaved caspase-1 and GSDMD-N were significantly decreased in the Ad-sh-IFNAR2 group compared with the Ad-sh-NC group (Fig. 4A). Furthermore, LDH release was significantly reduced following IFNAR2 knockdown

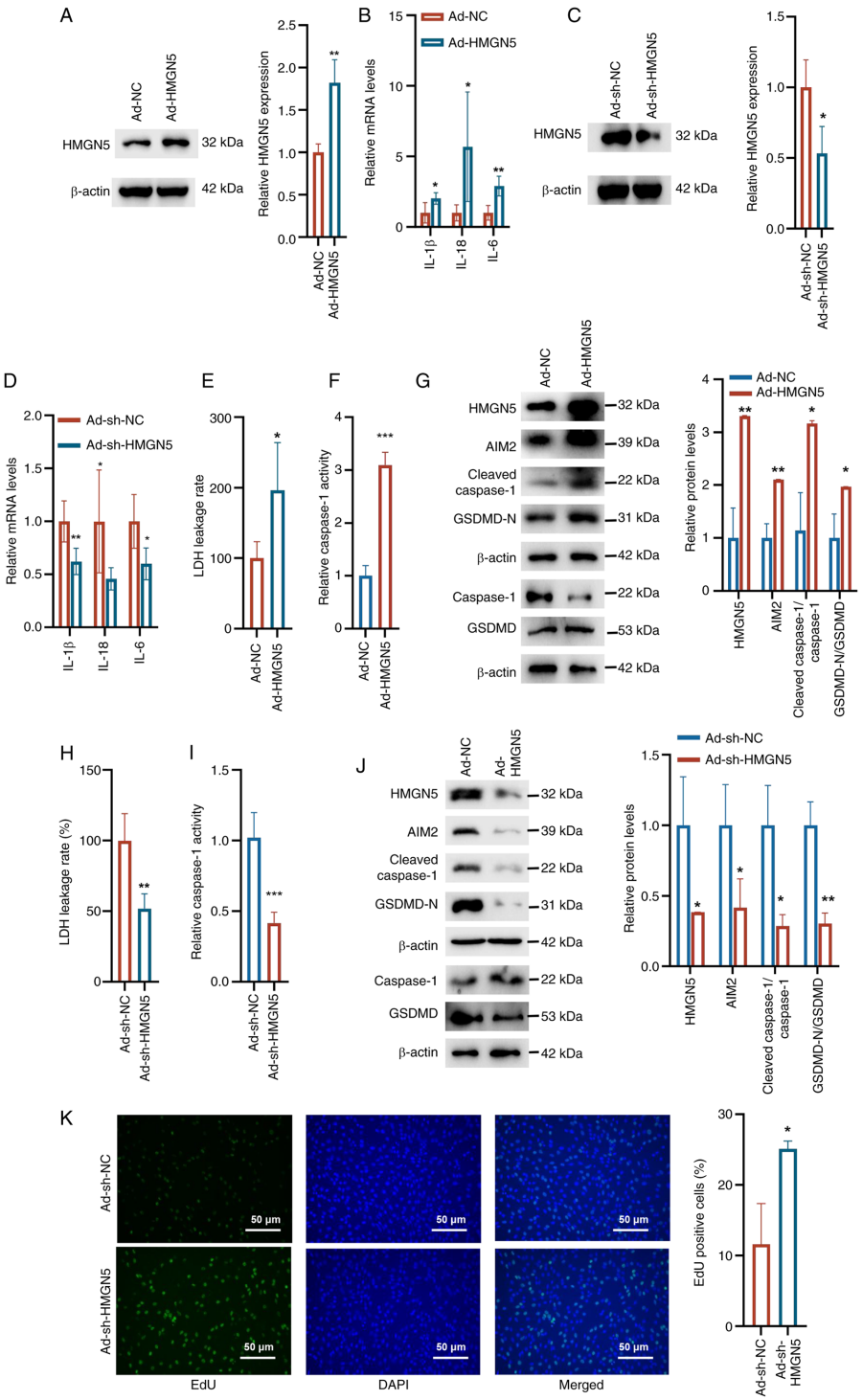


Figure 2. HMGN5 promotes the expression of pyroptosis-associated genes and modulates cell injury and proliferation in HK-2 cells. (A) Western blot analysis and semi-quantification of HMGN5 protein levels following the overexpression of HMGN5 using Ad-HMGN5, confirming the efficiency of HMGN5 overexpression. (B) Overexpression of HMGN5 significantly upregulated the mRNA levels of pro-inflammatory cytokines IL-1β, IL-18 and IL-6 compared with controls. *P<0.05 and **P<0.01 vs. Ad-NC. (C) Western blot analysis and semi-quantification of HMGN5 protein levels following the knockdown of HMGN5 using Ad-sh-HMGN5, confirming knockdown efficiency. (D) HMGN5 knockdown significantly reduced the expression of IL-1β, IL-18 and IL-6 at the mRNA level. *P<0.05 and **P<0.01 vs. Ad-sh-NC. (E) HMGN5 overexpression promoted LDH leakage, indicating an increase in cell injury compared with controls. (F) Caspase-1 activity assay demonstrated that HMGN5 overexpression enhanced inflammasome activation. (G) Western blot analysis and the semi-quantification of protein levels showed that HMGN5 overexpression increased the protein levels of HMGN5, AIM2, cleaved caspase-1 and GSDMD-N. *P<0.05, **P<0.01 and ***P<0.001 vs. Ad-NC. (H) HMGN5 knockdown reduced LDH release, suggesting that silencing HMGN5 attenuated cell injury. (I) Caspase-1 activity assay results revealed that HMGN5 knockdown suppressed inflammasome activation. (J) Western blot analysis and the semi-quantification of protein levels showed that HMGN5 knockdown decreased the protein levels of HMGN5, AIM2, cleaved caspase-1 and GSDMD-N. For western blot analyses, proteins and their corresponding controls were detected using the same batch of total protein samples, with β-actin serving as an internal loading control to ensure comparability. (K) Representative images of an EdU incorporation assay and the quantification of results, demonstrating that HMGN5 knockdown enhanced the proliferative capacity of HK-2 cells. Scale bar, 50 μm; *P<0.05, and **P<0.01 vs. Ad-sh-NC. Data are presented as mean ± SEM (n=3 independent biological replicates). HMGN5, high mobility group nucleosome-binding 5; AIM2, absent in melanoma 2; GSDMD, gasdermin D; GSDMD-N, N-terminal pore-forming domain of gasdermin D; LDH, lactate dehydrogenase; Ad-NC, negative control for overexpression; Ad-HMGN5, HMGN5 overexpression vector; Ad-sh-NC, negative control short hairpin RNA sequence; Ad-sh-HMGN5, short hairpin RNA sequence targeting HMGN5.

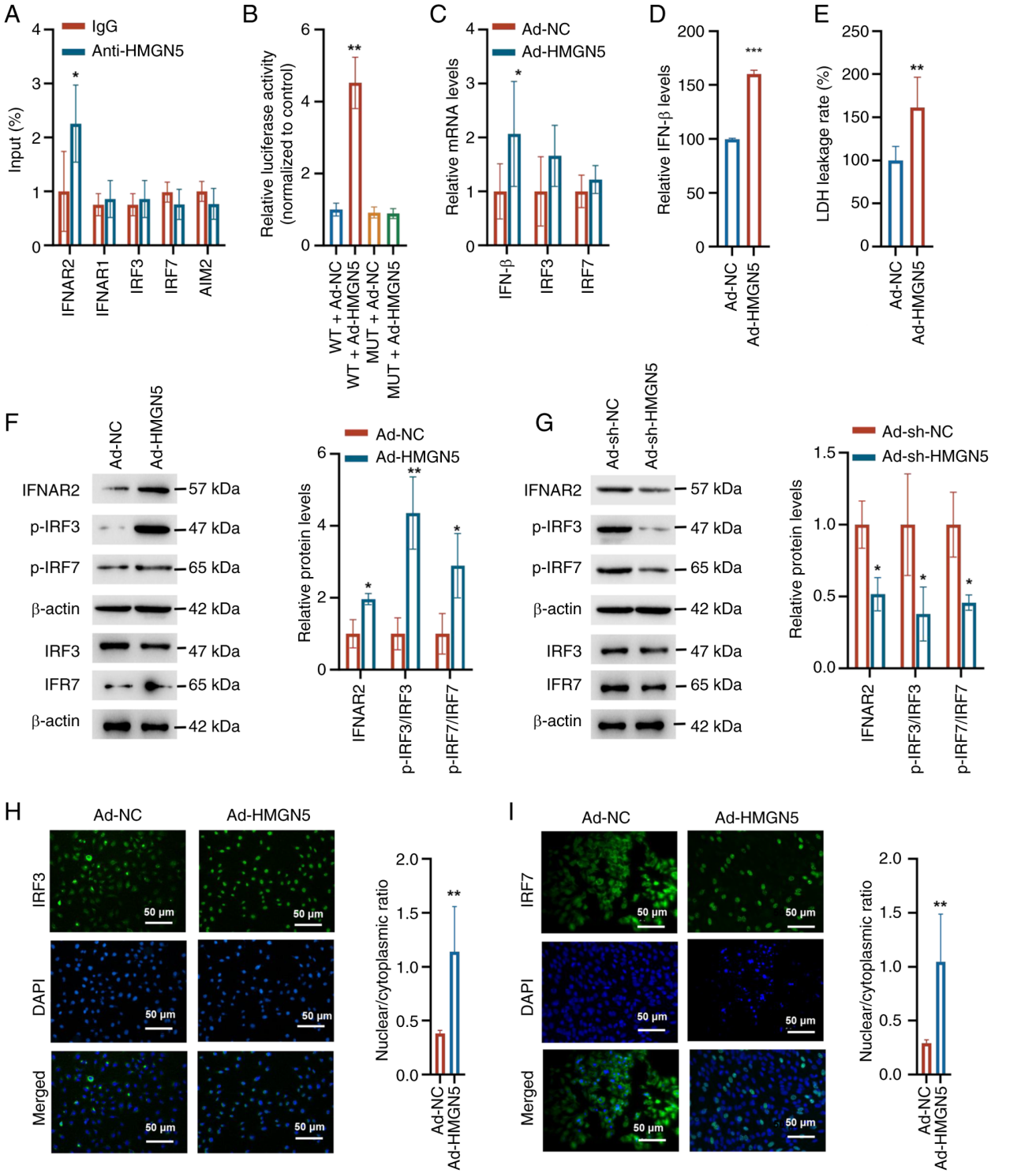


Figure 3. HMGN5 binds to the *IFNAR2* promoter and promotes its expression, leading to IRF3/IRF7 activation and nuclear translocation in HK-2 cells. (A) Chromatin immunoprecipitation-qPCR analysis showed HMGN5 enrichment at the promoter region of IFNAR2, with no significant changes in HMGN5 enrichment detected at the *AIM2*, *IFNAR1*, *IRF3* or *IRF7* promoters compared with the IgG control. *P<0.05 vs. IgG. (B) Dual-luciferase reporter assay in HK-2 cells evaluating the transcriptional activity of WT or MUT *IFNAR2* promoter constructs under HMGN5 overexpression. **P<0.01 vs. WT + Ad-NC. (C) Reverse transcription-qPCR analysis of *IFN-β*, *IRF7* and *IRF3* mRNA levels in HK-2 cells. *P<0.05 vs. Ad-NC. (D) ELISA analysis of IFN-β protein secretion. ***P<0.001 vs. Ad-NC. (E) LDH release assay in HK-2 cells showed that HMGN5 overexpression increased LDH release. **P<0.01 vs. Ad-NC. (F) Western blot analysis and semi-quantification of IFNAR2, p-IRF3, IRF3, p-IRF7 and IRF7 protein levels in HK-2 cells overexpressing HMGN5. *P<0.05 vs. Ad-NC. (G) Western blot analysis and semi-quantification of IFNAR2, p-IRF3, IRF3, p-IRF7 and IRF7 protein levels in HK-2 cells after HMGN5 knockdown. *P<0.05 vs. Ad-sh-NC. For western blot analyses, cleaved/phosphorylated proteins and their corresponding total protein forms were detected using the same batch of protein lysates in parallel experiments, with β-actin serving as an internal loading control to ensure comparability. Representative images of immunofluorescence staining showing the nuclear translocation of (H) IRF3 and (I) IRF7 in HK-2 cells, which were quantified to provide nuclear-to-cytoplasmic ratios of each protein. Scale bar, 50 μm; **P<0.01 vs. Ad-NC. Data are presented as mean ± SEM (n=3 independent biological replicates). HMGN5, high mobility group nucleosome-binding 5; IFNAR1, interferon receptor 1; IFNAR2, interferon receptor 2; qPCR, quantitative PCR; AIM2, absent in melanoma 2; IRF3, interferon regulatory factor 3; IRF7, interferon regulatory factor 7; WT, wild-type; MUT, mutant; IFN-β, interferon-β; LDH, lactate dehydrogenase; p-, phosphorylated-; Ad-NC, negative control for overexpression; Ad-HMGN5, HMGN5 overexpression vector; Ad-sh-NC, negative control short hairpin RNA sequence; Ad-sh-HMGN5, short hairpin RNA sequence targeting HMGN5.

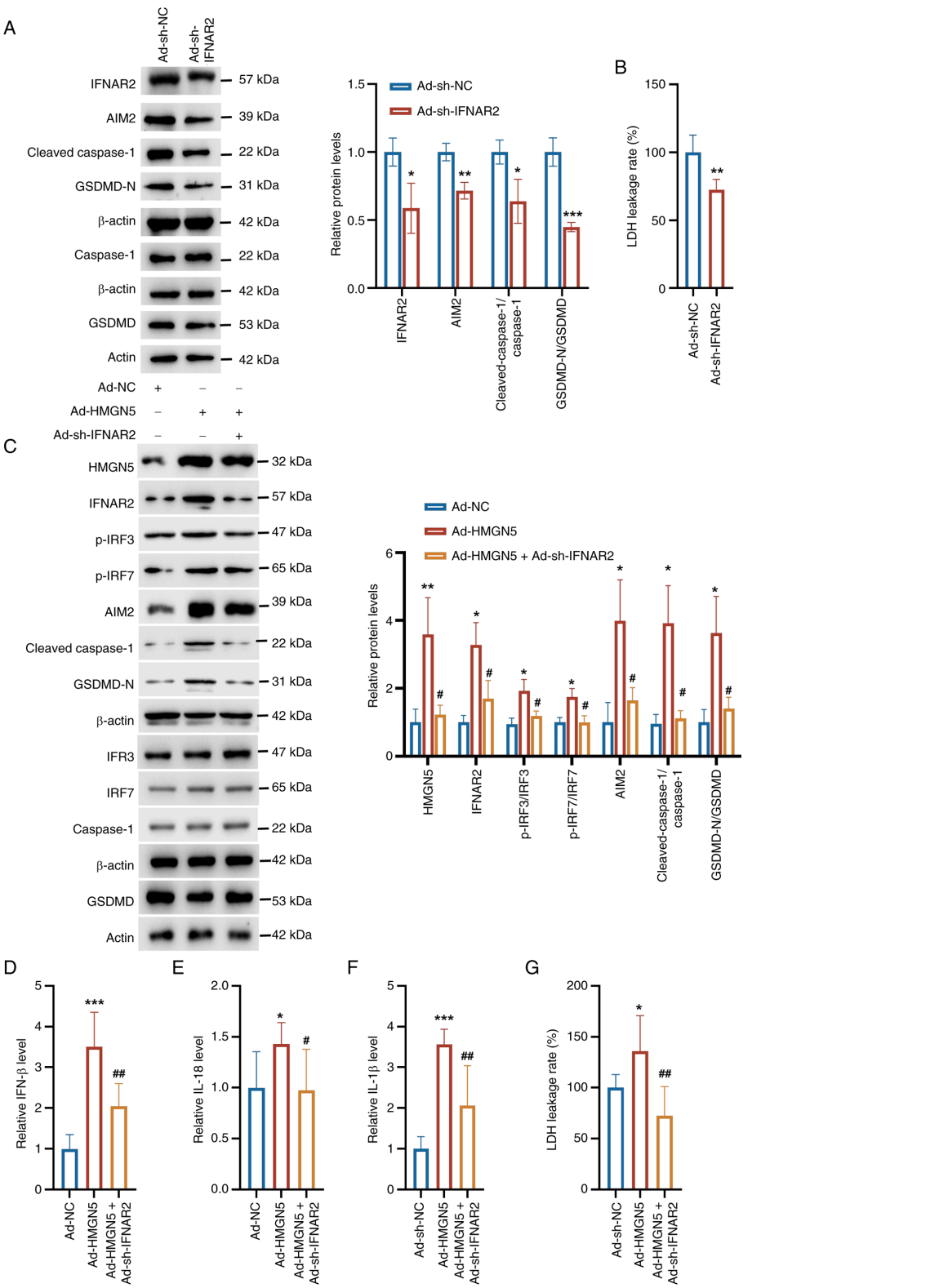


Figure 4. IFNAR2 signaling contributes to HMGN5-mediated pyroptosis-associated cellular responses in HK-2 cells. (A) Western blot analysis and semi-quantification of IFNAR2, AIM2, caspase-1, cleaved caspase-1, GSDMD and GSDMD-N protein levels in HK-2 cells following *IFNAR2* knockdown. (B) LDH release assay in HK-2 cells showed that *IFNAR2* knockdown reduced LDH release. *P<0.05 and **P<0.01 vs. Ad-sh-NC. (C) Western blot analysis and semi-quantification of HMGN5, IFNAR2, IRF3, p-IRF3, IRF7, p-IRF7, AIM2, caspase-1, cleaved caspase-1, GSDMD and GSDMD-N protein levels in HK-2 cells overexpressing HMGN5, with or without concurrent *IFNAR2* knockdown. For western blot analyses, cleaved/phosphorylated proteins and their corresponding total protein forms were detected using the same batch of protein lysates in parallel experiments, with β-actin serving as an internal loading control to ensure comparability. ELISA analysis of (D) IFN-β, (E) IL-8 and (F) IL-1β secretion in HK-2 cells overexpressing HMGN5, with or without concurrent *IFNAR2* knockdown. (G) LDH release assay in HK-2 cells overexpressing HMGN5, with or without concurrent *IFNAR2* knockdown. Data are presented as mean ± SEM (n=3 independent biological replicates). *P<0.05, **P<0.01 and ***P<0.001 vs. Ad-NC; $^{\#}$P<0.05 and $^{\#\#}$P<0.01 vs. Ad-HMGN5. IFNAR2, interferon receptor 2; HMGN5, high mobility group nucleosome-binding 5; AIM2, absent in melanoma 2; GSDMD, gasdermin D; GSDMD-N, N-terminal pore-forming domain of gasdermin D; IRF3, interferon regulatory factor 3; IRF7, interferon regulatory factor 7; IFN-β, interferon-β; LDH, lactate dehydrogenase; p-, phosphorylated-; Ad-sh-NC, negative control short hairpin RNA sequence; Ad-sh-IFNAR2, short hairpin RNA sequence targeting IFNAR2; Ad-NC, negative control for overexpression; Ad-HMGN5, HMGN5 overexpression vector.

compared with the control group (Fig. 4B), indicating that IFNAR2 knockdown attenuated membrane damage, which was consistent with the suppression of pyroptosis-associated signaling.

Subsequently, the present study examined whether HMGN5 regulated HK-2 cell injury through an IFNAR2-dependent mechanism. HMGN5 overexpression significantly increased the expression of IFNAR2, p-IRF3, p-IRF7, AIM2, cleaved caspase-1 and GSDMD-N compared with Ad-NC-treated cells (Fig. 4C). Notably, concurrent IFNAR2 knockdown partially yet significantly reversed the HMGN5-induced upregulation of these proteins (Fig. 4C), suggesting that IFNAR2 signaling was a key mediator required for HMGN5-induced activation of the AIM2 inflammasome and downstream pyroptosis-associated signaling cascades. In parallel, ELISA analyses demonstrated that, compared with controls, HMGN5 overexpression significantly increased the secretion of IL-1β, IL-8 and IFN-β. Furthermore, silencing IFNAR2 significantly mitigated these HMGN5-induced elevations (Fig. 4D-F), suggesting that the HMGN5-IFNAR2 axis contributed to downstream pyroptosis-associated signaling in renal tubular cells. Additionally, compared with the control group, a significant increase in LDH release was induced by HMGN5 overexpression; this elevation in LDH leakage was significantly reduced by concurrent IFNAR2 silencing (Fig. 4G), further supporting an important role for IFNAR2 signaling in mediating HMGN5-modulated pyroptosis-associated cell injury.

HMGN5 expression and pyroptosis-associated signaling are upregulated in the kidneys of CKD-model mice. To establish a mouse model of CKD, mice were subjected to a two-step nephrectomy involving an initial left total nephrectomy followed by a right partial (2/3) nephrectomy 1 week later. Histopathological analysis using H&E staining and Masson's trichrome staining revealed structural alterations in the renal tissue of CKD-model mice compared with sham-operated controls, with renal injury scores and fibrotic quantification indicating the occurrence of significant damage and fibrosis in model mice (Fig. 5A). Similarly, immunofluorescence staining demonstrated a significant increase in CTGF expression in the kidneys of CKD-model mice compared with control mice (Fig. 5B). Biochemical analyses further showed that plasma levels of creatinine and blood urea nitrogen were significantly elevated in CKD-model mice compared with sham-operated controls, providing further evidence of impaired renal function in the model (Fig. 5C and D). In parallel, circulating levels of IFN-β, IL-8 and IL-1β were significantly increased in CKD-model mice relative to the sham group (Fig. 5E-G), suggesting that model mice experienced enhanced systemic inflammatory and IFN responses. Additionally, LDH release assays revealed a significant increase in LDH leakage in renal tissue samples from CKD-model mice compared with sham controls (Fig. 5H), indicating that model mice experienced an increase in renal cell injury associated with pyroptosis-related signaling. At the molecular level, western blot analysis demonstrated that the protein expression levels of HMGN5, IFNAR2, cleaved caspase-1 and GSDMD-N were significantly elevated in the kidneys of CKD-model mice relative to sham-operated mice (Fig. 5I), suggesting that HMGN5-mediated activation of the IFNAR2 signaling axis may have contributed to the activation of pyroptosis-related pathways in CKD-model renal tissues.

IFNAR2 blockade attenuates renal injury and suppresses pyroptosis-associated signaling in CKD-model mice. To evaluate the pathophysiological impact of IFNAR blockade *in vivo*, CKD-model mice were treated with an IFNAR Ab. Histopathological examinations using H&E staining and Masson's trichrome staining revealed that IFNAR Ab treatment attenuated renal pathological alterations and significantly reduced fibrosis compared with untreated CKD-model mice (Fig. 6A). Consistent with these histological improvements, biochemical analyses demonstrated that, compared with the CKD-model group, plasma creatinine and urea levels were significantly reduced following IFNAR Ab treatment (Fig. 6B and C), indicating that this treatment improved renal function in CKD-model mice. In parallel, immunofluorescence staining showed that CTGF expression was significantly reduced in the renal tissues of IFNAR Ab-treated CKD-model mice compared with untreated CKD mice (Fig. 6D). ELISA analyses further revealed that IFNAR Ab treatment significantly reduced the circulating levels of IL-1β, IL-8 and IFN-β in CKD-model mice (Fig. 6E-G), suggesting that this treatment attenuated systemic inflammatory and type I IFN responses. Furthermore, LDH release assays demonstrated that IFNAR Ab treatment significantly reduced LDH leakage in renal tissues compared with CKD-model mice (Fig. 6H), indicating that this treatment attenuated renal cell injury associated with pyroptosis-related signaling. At the molecular level, western blot analysis showed that IFNAR Ab treatment partially yet significantly reversed the upregulation of IFNAR2, cleaved caspase-1 and GSDMD-N observed in the kidneys of CKD-model mice (Fig. 6I), suggesting the suppression of IFNAR2-associated pyroptosis-related signaling *in vivo*.

Discussion

CKD is characterized by persistent inflammation, tubular epithelial injury and progressive fibrosis, which drive the gradual loss of renal function (26). Increasing evidence has indicated that dysregulated innate immune signaling and sustained activation of inflammatory pathways contribute to CKD progression (1,2). However, the upstream nuclear events that link cellular stress to inflammatory amplification in renal tubular epithelial cells remain incompletely elucidated.

HMGN proteins are non-histone chromatin-binding proteins that function by competing with histone H1 for nucleosome binding, thereby reducing the compaction of chromatin and increasing the accessibility of regulatory DNA sequences for binding by transcription factors and RNA polymerase II (27). By modifying the global chromatin landscape, HMGN5 facilitates a permissive epigenetic state, enabling the efficient recruitment of transcriptional machinery to specific promoters. Additionally, a previous study identified HMGN1 as an endogenous alarmin capable of modulating innate immune responses (17). In particular, HMGN1 has been shown to synergize with Toll-like receptor 7/8 agonists to facilitate the activation of dendritic cells, promoting the nuclear translocation of IRF3 and IRF7 and the subsequent production of type I IFNs, including IFN-β (17). In systemic lupus erythematosus,

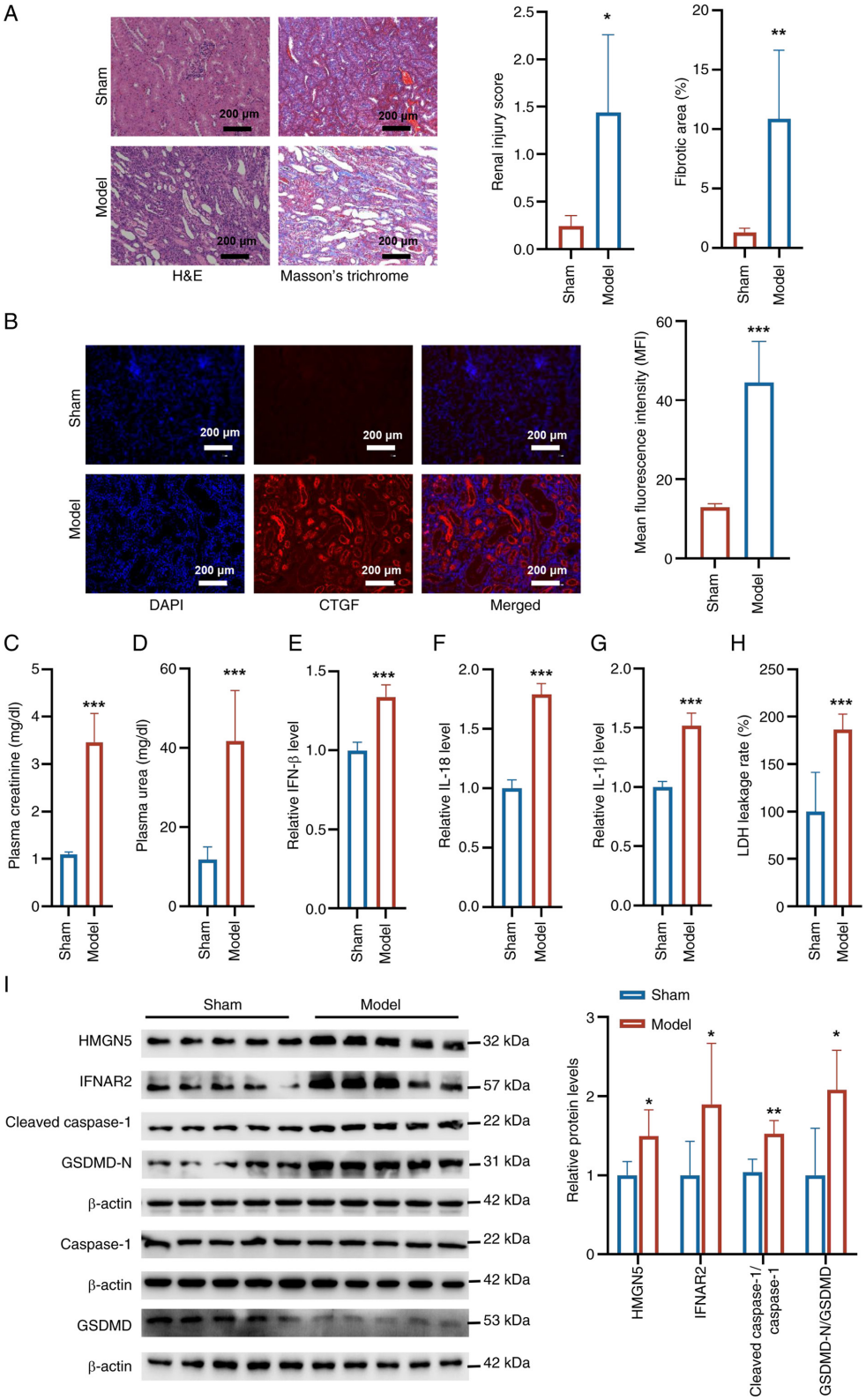


Figure 5. HMGN5 expression and pyroptosis-associated signaling are increased in the kidneys of CKD-model mice. (A) Representative images of H&E staining and Masson's trichrome staining in renal tissues from CKD-model mice and sham-operated controls. H&E staining was semi-quantified to calculate renal injury scores, and Masson's trichrome staining was used to quantify fibrosis in renal tissues. (B) Representative immunofluorescence staining images and quantification of CTGF expression in the renal tissues of mice from CKD-model and sham-operated groups. Plasma levels of (C) creatinine and (D) urea in CKD-model mice and sham-operated controls. ELISA analysis of plasma levels of (E) IFN-β, (F) IL-8 and (G) IL-1β. (H) Results of an LDH release assay performed on the renal tissues of CKD-model mice and sham-operated controls. (I) Western blot analysis and semi-quantification of HMGN5, IFNAR2, caspase-1, cleaved caspase-1, GSDMD and GSDMD-N protein levels in the renal tissues of CKD-model mice and sham-operated controls. For western blot analyses, cleaved/phosphorylated proteins and their corresponding total protein forms were detected using the same batch of protein lysates in parallel experiments, with β-actin serving as an internal loading control to ensure comparability. Scale bar, 200 μm. Data are presented as mean ± SEM (n=5 mice per group; 3 independent serial sections per sample). *P<0.05, **P<0.01 and ***P<0.001 vs. sham group. CKD, chronic kidney disease; H&E, hematoxylin and eosin; IFNAR2, interferon receptor 2; HMGN5, high mobility group nucleosome-binding 5; GSDMD, gasdermin D; GSDMD-N, N-terminal pore-forming domain of gasdermin D; IFN-β, interferon-β; LDH, lactate dehydrogenase; CTGF, connective tissue growth factor.

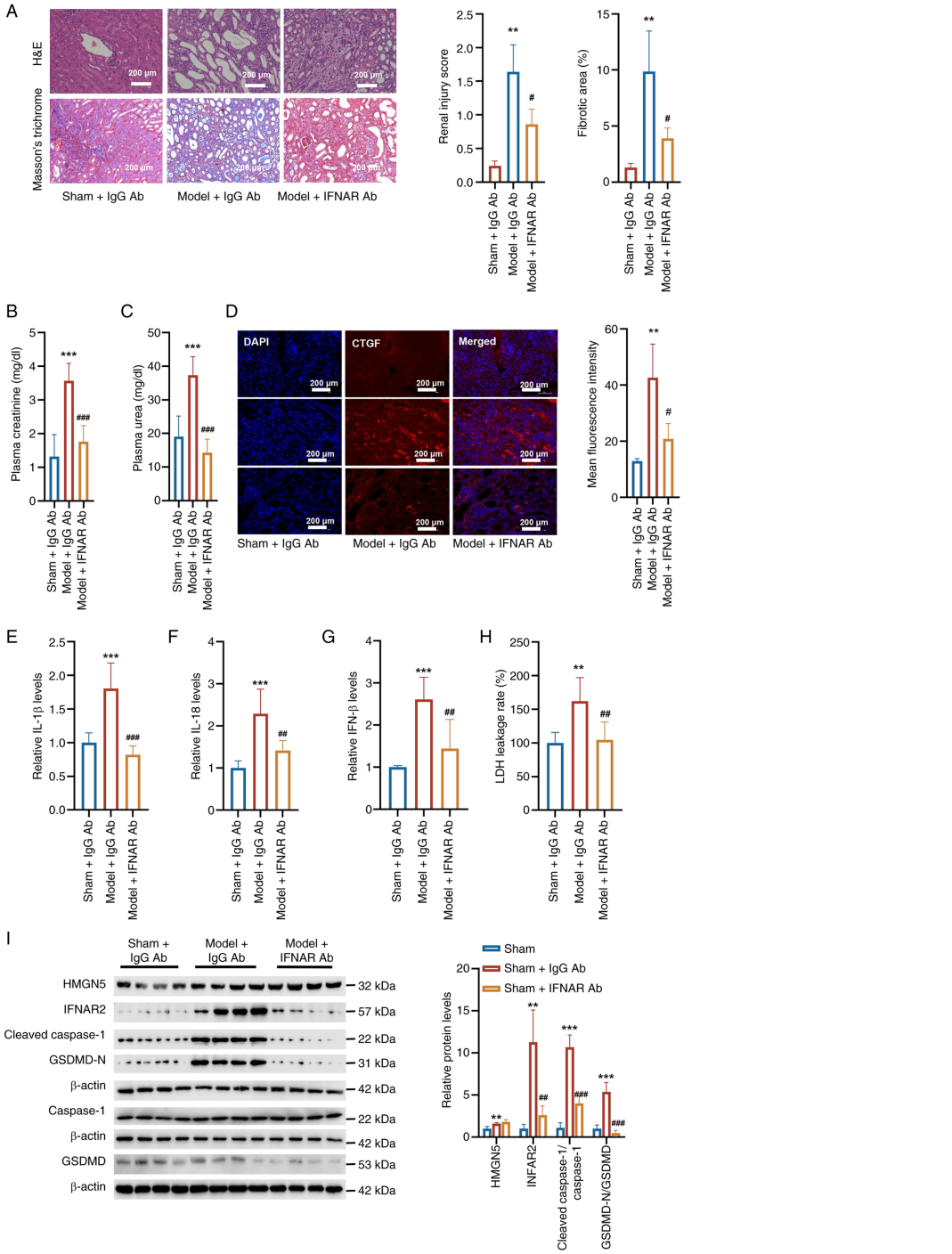


Figure 6. IFNAR Ab treatment partially attenuates renal injury and suppresses pyroptosis-associated changes in CKD-model mice. (A) Representative images of H&E staining and Masson's trichrome staining showing that IFNAR Ab treatment markedly attenuated renal pathological alterations and reduced fibrosis in CKD-model mice compared with untreated CKD-model controls. H&E staining was semi-quantified to calculate renal injury scores, and Masson's trichrome staining was used to quantify fibrosis in renal tissues. (B) Biochemical analysis showed that plasma creatinine levels were significantly decreased in CKD-model mice after IFNAR Ab treatment compared with the untreated CKD-model group. However, IFNAR Ab treatment did not completely restore plasma creatinine to control levels (C) Biochemical analysis revealed that plasma urea levels were significantly reduced, partially reversing the increase observed in untreated CKD-model mice, following IFNAR Ab treatment. (D) Representative immunofluorescence staining images and subsequent fluorescence-intensity quantification showed that CTGF expression was partially yet significantly reduced in the kidneys of IFNAR Ab-treated CKD-model mice compared with the untreated CKD-model group. ELISA analysis demonstrated that the plasma levels of (E) IL-1β, (F) IL-8 and (G) IFN-β were significantly attenuated in CKD-model mice after IFNAR Ab treatment compared with untreated CKD-model control mice. (H) LDH release assay results showed that LDH leakage in renal tissues was significantly reduced in CKD-model mice following IFNAR Ab treatment compared with the untreated CKD-model group. (I) Western blot analysis and semi-quantification demonstrated that the protein expression levels of IFNAR2, cleaved caspase-1 and GSDMD-N significantly decreased in the kidneys of IFNAR Ab-treated CKD-model mice compared with untreated CKD-model mice; however, the expression of these proteins was not fully restored to basal levels following this treatment. For western blot analyses, cleaved/phosphorylated proteins and their corresponding total protein forms were detected using the same batch of protein lysates in parallel experiments, with β-actin serving as an internal loading control to ensure comparability. Scale bar, 200 μm. Data are presented as mean ± SEM (n=5 mice per group; 3 independent serial sections per sample). **P<0.01 and ***P<0.001 vs. sham + IgG group; $^{\#}$P<0.05, $^{\#\#}$P<0.01 and $^{\#\#\#}$P<0.001 vs. model + IgG group. CKD, chronic kidney disease; H&E, hematoxylin and eosin; IFN-β, interferon-β; IFNAR, interferon receptor; IFNAR Ab, IFNAR-neutralizing antibody; LDH, lactate dehydrogenase; HMGN5, high mobility group nucleosome-binding 5; GSDMD, gasdermin D; GSDMD-N, N-terminal pore-forming domain of gasdermin D; CTGF, connective tissue growth factor.

HMGN family proteins have been implicated as molecular links between aberrant chromatin remodeling and IFN-associated inflammation (28). These findings highlight the potential for HMGN family members to serve as bridges between chromatin remodeling and inflammatory responses.

HMGN5 shares structural and functional similarities with HMGN1, including nucleosome-binding capacity and transcriptional regulatory potential (29), yet its role in non-immune parenchymal cells and chronic inflammatory diseases has remained largely unexplored. Given the importance of IFN signaling and innate immune activation in CKD, we hypothesized that HMGN5 may function as an upstream nuclear regulator that links chromatin dynamics to IFN-dependent inflammatory pathways in renal tubular epithelial cells.

The present study demonstrated that HMGN5 expression was elevated in renal tissues from patients with CKD and CKD-model mice, at both transcriptional and protein levels. This upregulation associated with structural damage, increased CTGF expression and indicators of inflammation (such as IL-8 and IL-1β) and renal dysfunction, suggesting that HMGN5 was closely associated with CKD progression. Mechanistically, the *in vitro* experiments of the present study revealed that HMGN5 overexpression in HK-2 cells promoted the expression of pyroptosis-associated molecules, including AIM2, cleaved caspase-1 and GSDMD-N; this upregulation was accompanied by increased LDH release and pro-inflammatory cytokine secretion.

Pyroptosis-associated signaling has been increasingly recognized as an important mechanism contributing to tubular injury, inflammatory amplification and fibrosis in CKD (25,30). Several lines of evidence from diverse disease contexts have supported the involvement of IFN signaling in pyroptosis-related pathways (12,31,32). For instance, granzyme A from cytotoxic lymphocytes has been shown to induce GSDMB-mediated pyroptosis in an IFN-dependent manner, highlighting a link between IFN signaling and GSDM-mediated inflammatory cell death (31). Similarly, IFN-γ has been shown to promote pyroptosis-related signaling in corneal epithelial cells through Janus kinase 2 (JAK2)/STAT1 activation, suggesting that type II IFNs can prime non-immune cells for inflammatory injury (12). In cancer models, the potentiation of type I IFN signaling through ubiquitin specific protease 18 depletion has been shown to induce pyroptosis-related signaling via STAT2- and NF-κB-dependent transcriptional programs, underscoring a broader role for IFN pathways in orchestrating inflammatory cell death (32). Regarding immune cells, AIM2 inflammasome activation and pyroptosis-related pathways in monocytes have been shown to be regulated by IFN-γ through the JAK2/STAT1 pathway, supporting the concept that IFN signaling contributes to inflammasome-mediated cell death across diverse cell types (9). Even during bacterial infection, type I IFNs have been shown to epigenetically upregulate pyroptosis-related genes, including *GSDMD*, further activating inflammasomes (33). Collectively, these studies have provided mechanistic and translational support for the findings of the present study, specifically that IFNAR2-dependent signaling contributed to HMGN5-mediated pyroptosis-associated cell injury in renal tubular epithelial cells.

Building upon these distinctions in inflammatory cell death pathways, it is important to further contextualize these findings: While apoptosis represents a non-inflammatory mode of programmed cell death characterized by cellular shrinkage and membrane blebbing without rupture, pyroptosis is a notably pro-inflammatory process driven by GSDM-mediated pore formation in the plasma membrane. This pore formation results in the rapid release of intracellular contents, for example LDH and pro-inflammatory cytokines, which markedly amplifies the inflammatory microenvironment (34). Previous studies have highlighted the notable role of GSDM in renal injury, demonstrating that GSDMD cleavage is a central executioner of pyroptosis in various renal pathologies, including acute kidney injury and diabetic nephropathy (34,35). Furthermore, the epigenetic control of inflammasomes has emerged as an important layer of regulation in pyroptosis; for instance, histone modification and chromatin remodeling have been shown to determine the transcriptional readiness of the NLRP3 and AIM2 loci (36-38). The findings of the present study extended this concept by proposing that HMGN5 serves as an epigenetic rheostat, precisely tuning the transcriptional activation of the *IFNAR2* promoter to facilitate downstream inflammasome assembly.

A key finding of the present study was the identification of IFNAR2-dependent signaling as a primary pathway mediating HMGN5-induced pyroptosis-associated responses. ChIP-qPCR assays demonstrated that HMGN5 was enriched at the *IFNAR2* promoter, suggesting a direct role in its transcriptional regulation. Similarly, HMGN5 overexpression enhanced IFNAR2 expression, promoted IRF3 and IRF7 phosphorylation and nuclear translocation, and increased IFN-β production in HK-2 cells. Notably, *IFNAR2* silencing mitigated HMGN5-induced activation of the AIM2 inflammasome, reduced downstream caspase-1 activation and GSDMD-N cleavage, and attenuated LDH release and inflammatory cytokine secretion. These findings indicate that HMGN5 functioned upstream of the IFNAR2 signaling axis, and that intact IFNAR2 signaling contributed to HMGN5-mediated pyroptosis-associated responses.

From a translational perspective, the *in vivo* data obtained in the present study demonstrated that pharmacological blockade of IFNAR2 signaling contributed to the mitigation of renal injury and the suppression of pyroptosis-associated signaling in CKD-model mice. IFNAR2 antibody treatment was associated with improved renal histopathology, reduced fibrosis, restored renal function and decreased systemic inflammatory markers in renal tissues. These findings suggest that IFNAR2 signaling may represent a potential therapeutic target in the context of CKD pathogenesis. However, it should be acknowledged that the 5/6 nephrectomy CKD mouse model used in the present study primarily reflects a specific context of remnant-kidney injury and hemodynamic overload (39). Future studies utilizing alternative etiological models, such as diabetic nephropathy or unilateral ureteral obstruction, will be important for determining whether the HMGN5-IFNAR2-IRF-AIM2 axis represents a generalized mechanism across the biological heterogeneity of CKD.

Furthermore, without direct *in vivo* HMGN5 gain- or loss-of-function experiments, the upstream role of HMGN5 in regulating IFNAR2 in the CKD mouse model remains an observation that warrants further verification. To support this causal link *in vivo*, future investigations utilizing tubule-specific *HMGN5*-knockout mice are warranted.

Although directly targeting chromatin-binding proteins, such as HMGN5, presents notable translational challenges, the results of the present study suggest that the modulation of IFNAR2 signaling could be explored as a theoretical strategy to attenuate IFN-driven and pyroptosis-related injury in CKD. Given that type I IFN pathways are already under investigation as therapeutic targets in autoimmune and inflammatory diseases (40,41), further research is required to evaluate whether IFNAR2-targeted approaches could eventually hold promise for attenuating progression in a subset of patients with inflammation-driven CKD.

Collectively, the findings of the present study identified HMGN5 as a potential epigenetic regulator associated with IFN-related inflammatory signaling in CKD. The data in the present study suggest that HMGN5 may have regulated *IFNAR2* expression via promoter enrichment and that *IFNAR2* knockdown mitigated HMGN5-induced pyroptosis-associated responses. The proposed HMGN5-IFNAR2-IRF3/IRF7-AIM2 pathway should be interpreted as a mechanistically supported pathway in CKD pathogenesis rather than an established signaling cascade. Further studies employing targeted gain- and loss-of-function approaches for IRF3, IRF7 and AIM2 will be required to define the precise downstream signaling hierarchy of this pathway. As such, the HMGN5-IFNAR2 axis warrants further investigation as a theoretical target for limiting pyroptosis-associated renal injury in CKD.

Acknowledgements

Not applicable.

Funding

The present study was supported by Hebei Provincial Institute of Medical Research (grant no.20241271).

Availability of data and materials

The data generated in the present study may be requested from the corresponding author.

Authors' contributions

XR, JX and LN designed the research, analyzed the data, performed the experiments, wrote the original draft of the manuscript and were responsible for making revisions to the manuscript. JZ, QZ, JW and GZ contributed to performing the animal experiments. LN secured funding. All authors confirm the authenticity of all the raw data. All authors read and approved the final version of the manuscript.

Ethics approval and consent to participate

The study protocol was approved by the Medical Scientific Research Ethics Committee of Shijiazhuang People's Hospital (Shijiazhuang, China; approval no. 2023-56A). Written informed consent was received for the patient study. All animal procedures were approved by the Medical Scientific Research Ethics Committee of Shijiazhuang People's Hospital (approval no. 2024-99).

Patient consent for publication

Not applicable.

Competing interests

The authors declare that they have no competing interests.

Use of artificial intelligence tools

During the preparation of this work, artificial intelligence tools (DeepSeek) were used to improve the readability and language of the manuscript, and subsequently, the authors revised and edited the content produced by the artificial intelligence tools as necessary, taking full responsibility for the ultimate content of the present manuscript.

References

1. Rao IR, Bangera A, Nagaraju SP, Shenoy SV, Prabhu RA, Rangaswamy D and Bhojaraja MV: Chronic kidney disease of unknown aetiology: A comprehensive review of a global public health problem. Trop Med Int Health 28: 588-600, 2023.
2. Kishi S, Nagasu H, Kidokoro K and Kashihara N: Oxidative stress and the role of redox signalling in chronic kidney disease. Nat Rev Nephrol 20: 101-119, 2024.
3. Zhu H, Cao C, Wu Z, Zhang H, Sun Z, Wang M, Xu H, Zhao Z, Wang Y, Pei G, *et al*: The probiotic L. casei Zhang slows the progression of acute and chronic kidney disease. Cell Metab 33: 1926-1942.e8, 2021.
4. Jiayi H, Ziyuan T, Tianhua X, Mingyu Z, Yutong M, Jingyu W, Hongli Z and Li S: Copper homeostasis in chronic kidney disease and its crosstalk with ferroptosis. Pharmacol Res 202: 107139, 2024.
5. Sanz AB, Sanchez-Niño MD, Ramos AM and Ortiz A: Regulated cell death pathways in kidney disease. Nat Rev Nephrol 19: 281-299, 2023.
6. Pang Q, Wang P, Pan Y, Dong X, Zhou T, Song X and Zhang A: Irisin protects against vascular calcification by activating autophagy and inhibiting NLRP3-mediated vascular smooth muscle cell pyroptosis in chronic kidney disease. Cell Death Dis 13: 283, 2022.
7. Ding B, Ma G, Wang Z, Liang W and Gao W: Mechanisms of kidney cell pyroptosis in chronic kidney disease and the effects of traditional chinese medicine. Evid Based Complement Alternat Med 2021: 1173324, 2021.
8. Chen Y, Ye X, Escames G, Lei W, Zhang X, Li M, Jing T, Yao Y, Qiu Z, Wang Z, *et al*: The NLRP3 inflammasome: Contributions to inflammation-related diseases. Cell Mol Biol Lett 28: 51, 2023.
9. Zhao Y, Liang B, Sheng S, Wang C, Jin B, Zhang X, Cheng Y, Shen C and Zheng F: AIM2 inflammasome regulated by the IFN-γ/JAK2/STAT1 pathway promotes activation and pyroptosis of monocytes in coronary artery disease. Immun Inflamm Dis 12: e1317, 2024.
10. Zhang Q, Meng Y, Zhao W, Li W, Dai C, Cheng J, Li B, Chen F, Yang J, Li H and Li S: IFN-γ-induced AIM2-PANoptosis in granulosa cells leads to ovulatory dysfunction in polycystic ovary syndrome. Biochem Pharmacol 250: 118039, 2026.
11. Costa Franco MMS, Marim FM, Alves-Silva J, Cerqueira D, Rungue M, Tavares IP and Oliveira SC: AIM2 senses Brucella abortus DNA in dendritic cells to induce IL-1β secretion, pyroptosis and resistance to bacterial infection in mice. Microbes Infect 21: 85-93, 2019.
12. Yang X, Zuo X, Zeng H, Liao K, He D, Wang B and Yuan J: IFN-γ facilitates corneal epithelial cell pyroptosis through the JAK2/STAT1 pathway in dry eye. Invest Ophthalmol Vis Sci 64: 34, 2023.
13. Luo L, Liu M, Fan Y, Zhang J, Liu L, Li Y, Zhang Q, Xie H, Jiang C, Wu J, *et al*: Intermittent theta-burst stimulation improves motor function by inhibiting neuronal pyroptosis and regulating microglial polarization via TLR4/NFkappaB/NLRP3 signaling pathway in cerebral ischemic mice. J Neuroinflammation 19: 141, 2022.

14. Jiang J, Shen W, He Y, Liu J, Ouyang J, Zhang C and Hu K: Overexpression of NLRP12 enhances antiviral immunity and alleviates herpes simplex keratitis via pyroptosis/IL-18/IFN-γ signaling. Int Immunopharmacol 137: 112428, 2024.
15. Mou J, Huang M, Wang F, Xu X, Xie H, Lu H, Li M, Li Y, Kong W, Chen J, *et al*: HMGN5 escorts oncogenic STAT3 signaling by regulating the chromatin landscape in breast cancer tumorigenesis. Mol Cancer Res 20: 1724-1738, 2022.
16. Rochman M, Malicet C and Bustin M: HMGN5/NSBP1: A new member of the HMGN protein family that affects chromatin structure and function. Biochim Biophys Acta 1799: 86-92, 2010.
17. Alam MM, Yang D, Trivett A, Meyer TJ and Oppenheim JJ: HMGN1 and R848 synergistically activate dendritic cells using multiple signaling pathways. Front Immunol 9: 2982, 2018.
18. Kulkarni HV, Mulay SR and Gaikwad AB: The AKI-CKD continuum: Mechanisms and therapeutic interventions. Nephrol Dial Transplant: Aug 8, 2026 (Epub ahead of print).
19. Hong W, Zhu Y, Lin Y, Tang S, Chen J, Xu L, Jiang J, Zong Y, Zhang Y, Sun A and Wu X: The chromatin remodeling protein BRG1 mediates Ang II induced pro-fibrogenic response in renal fibroblasts. Life Sci 340: 122320, 2024.
20. Kidney Disease: Improving Global Outcomes (KDIGO) CKD Work Group: KDIGO 2024 clinical practice guideline for the evaluation and management of chronic kidney disease. Kidney Int 105: S117-S314, 2024.
21. Hackstein CP, Spitzer J, Symeonidis K, Horvatic H, Bedke T, Steglich B, Klein S, Assmus LM, Odainic A, Szlapa J, *et al*: Interferon-induced IL-10 drives systemic T-cell dysfunction during chronic liver injury. J Hepatol 79: 150-166, 2023.
22. Huang MW, Stock AD, Mike EV, Herlitz L, Kolbeck R and Putterman C: Anti-IFNAR treatment does not reverse neuropsychiatric disease in MRL/lpr lupus mice. Lupus 28: 1510-1523, 2019.
23. Livak KJ and Schmittgen TD: Analysis of relative gene expression data using real-time quantitative PCR and the 2(-Delta Delta C(T)) method. Methods 25: 402-408, 2001.
24. Liu Y, Pan R, Ouyang Y, Gu W, Xiao T, Yang H, Tang L, Wang H, Xiang B and Chen P: Pyroptosis in health and disease: Mechanisms, regulation and clinical perspective. Signal Transduct Target Ther 9: 245, 2024.
25. Elias EE, Lyons B and Muruve DA: Gasdermins and pyroptosis in the kidney. Nat Rev Nephrol 19: 337-350, 2023.
26. Neuen BL, Yeung EK, Rangaswami J and Vaduganathan M: Combination therapy as a new standard of care in diabetic and non-diabetic chronic kidney disease. Nephrol Dial Transplant 40 (Suppl 1): i59-i69, 2025.
27. He B, Zhu I, Postnikov Y, Furusawa T, Jenkins L, Nanduri R, Bustin M and Landsman D: Multiple epigenetic factors co-localize with HMGN proteins in A-compartment chromatin. Epigenetics Chromatin 15: 23, 2022.
28. Lindblom J, Lagutkin D, Sherina N, Idborg H, Beretta L, Borghi MO; PRECISESADS Clinical Consortium; Peyper JM, Barturen G, Jakobsson PJ, *et al*: Novel IgG and IgA autoantibodies validated in two independent cohorts are associated with disease activity and determine organ manifestations in systemic lupus erythematosus: Implications for anti-LIN28A, anti-HMGN5, anti-IRF5, and anti-TGIF1. Ann Rheum Dis 84: 1164-1179, 2025.
29. Rodríguez-Ortiz A, Montoya-Villegas JC, García-Vallejo F and Mina-Paz Y: Spatial and temporal expression of high-mobility-group nucleosome-binding (HMGN) genes in brain areas associated with cognition in individuals with down syndrome. Genes (Basel) 12: 2000, 2021.
30. Wang Y, Li Y and Xu Y: Pyroptosis in kidney disease. J Mol Biol 434: 167290, 2022.
31. Zhou Z, He H, Wang K, Shi X, Wang Y, Su Y, Wang Y, Li D, Liu W, Zhang Y, *et al*: Granzyme A from cytotoxic lymphocytes cleaves GSDMB to trigger pyroptosis in target cells. Science 368: eaaz7548, 2020.
32. Arimoto KI, Miyauchi S, Troutman TD, Zhang Y, Liu M, Stoner SA, Davis AG, Fan JB, Huang YJ, Yan M, *et al*: Expansion of interferon inducible gene pool via USP18 inhibition promotes cancer cell pyroptosis. Nat Commun 14: 251, 2023.
33. Li Y, Guo X, Hu C, Du Y, Guo C, Wang D, Zhao W, Huang G, Li C, Lu Q, *et al*: Type I IFN operates pyroptosis and necroptosis during multidrug-resistant A. Baumannii infection. Cell Death Differ 25: 1304-1318, 2018.
34. Yu P, Zhang X, Liu N, Tang L, Peng C and Chen X: Pyroptosis: Mechanisms and diseases. Signal Transduct Target Ther 6: 128, 2021.
35. Zhang N, Zhang J, Yang Y, Shan H, Hou S, Fang H, Ma M, Chen Z, Tan L and Xu D: A palmitoylation-depalmitoylation relay spatiotemporally controls GSDMD activation in pyroptosis. Nat Cell Biol 26: 757-769, 2024.
36. Saller BS, Wöhrle S, Fischer L, Dufossez C, Ingerl IL, Kessler S, Mateo-Tortola M, Gorka O, Lange F, Cheng Y, *et al*: Acute suppression of mitochondrial ATP production prevents apoptosis and provides an essential signal for NLRP3 inflammasome activation. Immunity 58: 90-107.e11, 2025.
37. Fu M, Lan Z, Ye Y, Gong Y, Liang Q, Li M, Feng L, Chen A, Dong Q, Li Y, *et al*: The metabolite alpha-ketoglutarate inhibits vascular calcification partially through modulation of the TET2/NLRP3 inflammasome signaling pathway. Kidney Int 108: 233-252, 2025.
38. Li Y, Wang L, Wanga W, Wangb W, Huang W and Liu S: Acetylation modification of AIM2 by KAT2B suppresses the AKT/Wnt/β-catenin signaling pathway activation and inhibits breast cancer progression. Epigenetics Chromatin 18: 27, 2025.
39. Tan RZ, Zhong X, Li JC, Zhang YW, Yan Y, Liao Y, Wen D, Diao H, Wang L and Shen HC: An optimized 5/6 nephrectomy mouse model based on unilateral kidney ligation and its application in renal fibrosis research. Ren Fail 41: 555-566, 2019.
40. Goel RR, Kotenko SV and Kaplan MJ: Interferon lambda in inflammation and autoimmune rheumatic diseases. Nat Rev Rheumatol 17: 349-362, 2021.
41. Wu YY, Xing J, Li XF, Yang YL, Shao H and Li J: Roles of interferon induced protein with tetratricopeptide repeats (IFIT) family in autoimmune disease. Autoimmun Rev 22: 103453, 2023.

Copyright © 2026 Rong et al. This work is licensed under a Creative Commons Attribution-NonCommercial-NoDerivatives 4.0 International (CC BY-NC-ND 4.0) License.